

Magnonic Superradiant Phase Transition

Motoaki Bamba*

*Department of Physics, Kyoto University, Kyoto 606-8502, Japan and
PRESTO, Japan Science and Technology Agency, Kawaguchi 332-0012, Japan*

Xinwei Li

Department of Electrical and Computer Engineering, Rice University, Houston 77005, USA

Nicolas Marquez Peraca

Department of Physics and Astronomy, Rice University, Houston 77005, USA

Junichiro Kono

*Department of Electrical and Computer Engineering, Rice University, Houston 77005, USA
Department of Material Science and NanoEngineering, Rice University, Houston 77005, USA and
Department of Physics and Astronomy, Rice University, Houston 77005, USA*

(Dated: November 7, 2021)

We show that the low-temperature phase transition in ErFeO_3 that occurs at a critical temperature of ~ 4 K can be described as a magnonic version of the superradiant phase transition (SRPT). The role of photons in the quantum-optical SRPT is played by Fe^{3+} magnons, while that of two-level atoms is played by Er^{3+} spins. Our spin model, which is reduced to an extended Dicke model, takes into account the short-range, direct exchange interactions between Er^{3+} spins in addition to the long-range Er^{3+} - Er^{3+} interactions mediated by Fe^{3+} magnons. By using realistic parameters determined by recent terahertz magnetospectroscopy and magnetization experiments, we demonstrate that it is the cooperative, ultrastrong coupling between Er^{3+} spins and Fe^{3+} magnons that causes the phase transition. This work thus proves ErFeO_3 to be a unique system that exhibits a SRPT in thermal equilibrium, in contrast to previous observations of laser-driven non-equilibrium SRPTs.

I. INTRODUCTION

In 1973, it was proposed [1, 2] that a static transverse electromagnetic field (a *photon* field) and a static polarization (a *matter* field) spontaneously appear in thermal equilibrium, when the photon-matter coupling strength exceeds a certain threshold, entering the so-called ultrastrong coupling regime [3–5]. This phenomenon has come to be known as the superradiant phase transition (SRPT), or the Dicke phase transition, since the Dicke model (originally developed for the phenomenon of superradiance [6]) was used in the theoretical calculations [1, 2].

While the focus of optical science has traditionally been on non-equilibrium excited-state dynamics, a unique aspect of the SRPT is that it is concerned with the thermal-equilibrium state of a light-matter coupled system. Non-equilibrium SRPTs have been demonstrated in cold atom systems driven by laser light [7, 8], but realization of the SRPT in true thermal equilibrium has been challenging. The existence of an analog of the SRPT has been theoretically shown for a superconducting circuit in thermal equilibrium [9], but no experimental observations have been reported for this situation, either.

Early studies suggested no-go theorems against the SRPT [10–13] suggesting that the thermal-equilibrium

SRPT is impossible to realize in systems described by the minimal-coupling Hamiltonian, i.e., charged particles (without spins) interacting with electromagnetic fields. Since the classical treatment of the electromagnetic fields used in proofs of such no-go theorems can be justified only in limited situations [2, 12–16], proposals of counter-examples against the no-go theorems and criticisms against the counter-examples have been repeated in the research history of the SRPT [17–27].

One way to evade the no-go theorems is by introducing another degree of freedom, such as spin [11]. For example, it has been shown that the Rashba spin-orbit coupling can cause a paramagnetic instability in an ultrastrongly coupled system between a cyclotron resonance and a cavity photon field, implying a SRPT [27]. Another way is to utilize various types of interactions in magnetic materials, which cannot be described by the minimal-coupling Hamiltonian. Ultrastrong photon-magnon coupling has been reported [28–32], but evidence for a SRPT has not been achieved. A variety of phase transitions exist in magnetic systems, and it is conceivable that some of the known phase transitions can be understood as a realization of the SRPT. In this context, it is noteworthy that the problem of ultrastrong coupling between Er^{3+} spins and Fe^{3+} magnons in ErFeO_3 has been mapped to the Dicke model in a recent experimental study [33]. In this extraordinary situation of matter-matter ultrastrong coupling, the role of photons in the usual Dicke model is played by magnons.

In this paper, we theoretically show that the phase

* E-mail: bamba.motoaki.y13@kyoto-u.jp

transition in ErFeO_3 with a critical temperature (T_c) of ~ 4 K, known as the low-temperature phase transition (LTPT), is a magnonic SRPT, i.e., an analog of the SRPT where Er^{3+} spins cooperatively couple with a Fe^{3+} magnonic field, instead of a photonic field as in the originally proposed SRPT.

We determined the parameters in our spin model from terahertz magnetospectroscopy [33] and magnetization [34] experiments. We derived an extended version of the Dicke model [6] from the spin model and clarified the correspondence between the LTPT and the SRPT. We found that the LTPT can occur due to the Er^{3+} -magnon coupling even in the absence of direct Er^{3+} - Er^{3+} exchange interactions. Also, we observed that the critical temperature T_c of the LTPT is enhanced by the Er^{3+} -magnon coupling, compared to that obtained only by the direct Er^{3+} - Er^{3+} interactions. These results demonstrate that ErFeO_3 is a unique physical system in which a SRPT can be experimentally realized in thermal equilibrium.

This paper is organized as follows. We first review the SRPT in the Dicke model and the LTPT in ErFeO_3 in Secs. II and III, respectively. Our spin model of ErFeO_3 is described in Sec. IV. Calculated phase diagrams are shown in Sec. V. For discussing the analogy with the SRPT, an extended version of the Dicke model is derived from the spin model in Sec. VI. The analogy is fully discussed in Sec. VII. Section VIII summarizes our findings.

Appendix A shows the details of our mean-field calculation. In Appendix B, we show how the number of parameters in the spin model can be reduced by considering the low-temperature spin configuration in ErFeO_3 . In Appendix C, spin resonance frequencies are numerically calculated by the mean-field method and by the extended Dicke Hamiltonian for comparing these methods as well as for determining the parameters. In Appendix D, the actual values of the parameters are listed. In Appendix E, the magnon quantization procedure for the Fe^{3+} subsystem is described. In Appendix F, we discuss small differences of the phase diagrams between that obtained by the mean-field method and that obtained by the extended Dicke Hamiltonian.

II. SUPERRADIANT PHASE TRANSITION IN THE DICKE MODEL

The SRPT was first suggested in 1973 by Hepp and Lieb [1] and has been extensively discussed based on the Dicke model [6] expressed as

$$\frac{\hat{\mathcal{H}}_{\text{Dicke}}}{\hbar} \equiv \omega_{\text{ph}} \hat{a}^\dagger \hat{a} + \omega_{\text{ex}} \hat{S}_x + \frac{i2g}{\sqrt{N}} (\hat{a}^\dagger - \hat{a}) \hat{S}_z. \quad (1)$$

Here, \hat{a} is the annihilation operator of a photon in a photonic mode with a resonance frequency ω_{ph} , $\hat{S}_{x,y,z}$ are the spin- $\frac{N}{2}$ operators representing an ensemble of two-level atoms with a transition frequency ω_{ex} , and N is the number of atoms. The last term represents the cou-

pling between the photonic mode and the atomic ensemble with a strength of g . In the thermodynamic limit, i.e., $N \rightarrow \infty$, the SRPT arise when $4g^2 > \omega_{\text{ph}}\omega_{\text{ex}}$, i.e., in the ultrastrong coupling regime, $g \gtrsim \omega_{\text{ph}}, \omega_{\text{ex}}$ [3–5]. Below T_c , the expectation values of the photon annihilation operator $\langle \hat{a} \rangle$ and spin operator $\langle \hat{S}_z \rangle$ become nonzero, signaling the spontaneous appearance of a static electromagnetic field and a static polarization (or a persistent electric current) in thermal equilibrium.

A simpler calculation method for the SRPT was demonstrated by Wang and Hioe, also in 1973 [2], and its validity for the Dicke model was confirmed by Hepp and Lieb [14]. The partition function at temperature T

$$\mathcal{Z}_{\text{Dicke}}(T) \equiv \text{Tr}[e^{-\hat{\mathcal{H}}_{\text{Dicke}}/(k_{\text{B}}T)}] \quad (2)$$

in the thermodynamic limit, $N \rightarrow \infty$, can be approximately evaluated by replacing the trace over the photonic variables with an integral over coherent states $|\sqrt{N}\bar{a}\rangle$ ($\bar{a} \in \mathbb{C}$; giving $\hat{a}|\sqrt{N}\bar{a}\rangle = \sqrt{N}\bar{a}|\sqrt{N}\bar{a}\rangle$) as

$$\bar{\mathcal{Z}}_{\text{Dicke}}(T) \equiv \int \frac{d^2\bar{a}}{\pi/N} \text{Tr}[e^{-\hat{\mathcal{H}}_{\text{Dicke}}^{\text{eff}}(\bar{a})/(k_{\text{B}}T)}] \quad (3a)$$

$$= \int \frac{d^2\bar{a}}{\pi/N} e^{-\bar{\mathcal{S}}_{\text{Dicke}}(\bar{a}, T)/(k_{\text{B}}T)}, \quad (3b)$$

where we defined an effective Hamiltonian

$$\frac{\hat{\mathcal{H}}_{\text{Dicke}}^{\text{eff}}(\bar{a})}{\hbar} \equiv N\omega_{\text{ph}}|\bar{a}|^2 + \omega_{\text{ex}}\hat{S}_x + i2g(\bar{a}^* - \bar{a})\hat{S}_z, \quad (4)$$

an action

$$\bar{\mathcal{S}}_{\text{Dicke}}(\bar{a}, T) \equiv -k_{\text{B}}T \ln \text{Tr}[e^{-\hat{\mathcal{H}}_{\text{Dicke}}^{\text{eff}}(\bar{a})/(k_{\text{B}}T)}] \quad (5a)$$

$$= N \left\{ \hbar\omega_{\text{ph}}|\bar{a}|^2 - k_{\text{B}}T \ln \text{Tr}[e^{-\hat{\mathcal{H}}_{\text{Dicke}}^{\text{a}}(\bar{a})/(k_{\text{B}}T)}] \right\}, \quad (5b)$$

and an effective Hamiltonian per atom

$$\frac{\hat{\mathcal{H}}_{\text{Dicke}}^{\text{a}}(\bar{a})}{\hbar} \equiv \frac{\omega_{\text{ex}}}{2} \hat{\sigma}_x + ig(\bar{a}^* - \bar{a})\hat{\sigma}_z. \quad (6)$$

The normalized expectation value $\bar{a} = \langle \hat{a} \rangle / \sqrt{N}$ of the annihilation operator of a photon at temperature T can be determined for minimizing the action, i.e., $\partial\bar{\mathcal{S}}/\partial\text{Re}[\bar{a}] = 0$ and $\partial\bar{\mathcal{S}}/\partial\text{Im}[\bar{a}] = 0$. We find that \bar{a} acquires a nonzero value below T_c when $4g^2 > \omega_{\text{ph}}\omega_{\text{ex}}$ is satisfied ($\sqrt{N}\bar{a}$ gives a finite electric (displacement) field or vector potential even in the thermodynamic limit, $N \rightarrow \infty$, if the atomic density is fixed). The above approximation is justified if the free energy $\bar{\mathcal{F}}_{\text{Dicke}}(T) \equiv -(k_{\text{B}}T/N) \ln \bar{\mathcal{Z}}_{\text{Dicke}}(T)$ per atom satisfies $\hbar\omega_{\text{ph}}/N \ll |\bar{\mathcal{F}}_{\text{Dicke}}(T)|$ in the thermodynamic limit [12, 13, 15, 16].

Based on the above semiclassical calculation scheme, Rzążewski *et al.* derived no-go theorems starting from the minimal-coupling Hamiltonian in the long-wavelength approximation in 1979 [12] and in the general case in 1981 [13]. However, since the proof had the above-mentioned limitation of validity due to the semiclassical treatment employed, the presence of the SRPT in the minimal-coupling Hamiltonian is still controversial [17–27].

III. LOW-TEMPERATURE PHASE TRANSITION IN ErFeO_3

Resonance frequencies of magnons, quanta of spin waves, in magnetic materials have provided rich information on the spin configurations of materials. Softening (i.e., decrease of resonance frequency) of magnon modes has been discussed in connection with magnetic phase transitions. Magnons also provide a platform for electrodynamics studies both in the classical and quantum regimes [28–33, 35–42].

Due to the coupling (amplitude exchange) between a magnon in magnetic materials and a photon (electromagnetic wave) in a cavity, which can be described by the last term in the Dicke model [Eq. (1)], we can observe anticrossing on their resonance frequencies. If the anticrossing frequency is higher than dephasing rates (broadening or linewidth), we can exchange the amplitude coherently between the magnon and photon modes. Such a regime is called the strong coupling regime, and it attracts much attention for coherent transfer of quantum information between different media of quanta [28, 29, 35–38] and for magnon detection [32, 39, 42].

On the other hand, the anticrossing frequency ($2g$) can be comparable to the original resonance frequency (ω_{ph}) of photons, magnons, or other material excitations (ω_{ex}), i.e., the ultrastrong coupling regime [3–5]. Ultrastrong photon–magnon coupling has been reported for a yttrium-iron-garnet (YIG) sphere embedded in a cavity with a resonance frequency in the gigahertz (GHz) region [28–32]. Recently, $g/\omega \sim 0.46$ has been achieved for the purpose of detecting dark matter (galactic axions) [32, 39]. Ultrastrong spin–magnon [33] and magnon–magnon [40, 41] coupling have also been observed. Among such magnetic materials with ultrastrong coupling, ErFeO_3 is a candidate material showing the magnonic SRPT as explained below.

As shown in Fig. 1, at $T_c \sim 4$ K, ErFeO_3 shows the LTPT [43, 44], a second-order phase transition where Er^{3+} spins are ordered antiferromagnetically along the c axis together with a rotation of the Fe^{3+} antiferromagnetism (AFM) vector $\mathbf{S}^A - \mathbf{S}^B$ in the bc plane due to the Er^{3+} – Fe^{3+} exchange interactions.

In the absence of those exchange interactions, as in Fig. 1(a), Fe^{3+} spins are ordered antiferromagnetically just along the c axis with a slight canting to the a axis in the ground state of the Fe^{3+} subsystem. When we consider that the magnon excitation in this Fe^{3+} subsystem corresponds to the photon excitation in the electromagnetic vacuum, the rotation of the Fe^{3+} AFM vector (at $T < T_c$ as shown in Fig. 1(b)) means a spontaneous appearance of magnons, which corresponds to the appearance of photons (a static electromagnetic field) in the ordinary SRPT, in thermal equilibrium. The ordering of Er^{3+} spins correspond to the spontaneous appearance of an atomic field (a polarization) in the SRPT. In this way, we can expect that there is an analogy between the LTPT in ErFeO_3 and the SRPT in the Dicke model.

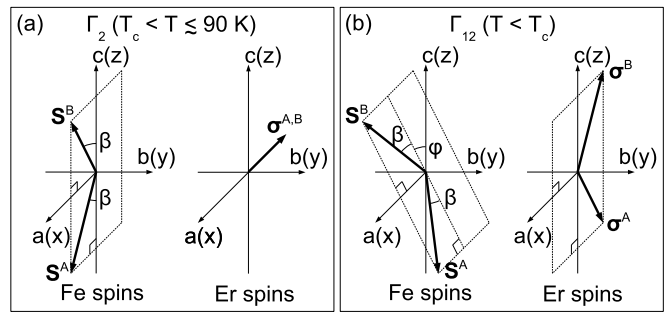


FIG. 1. Spin configurations in ErFeO_3 below and above $T_c \sim 4$ K. In this paper, we consider two-sublattice models both for Er^{3+} and Fe^{3+} spins. (a) In the high-temperature ($T_c < T \lesssim 90$ K, Γ_2) phase, the Fe^{3+} spins are ordered antiferromagnetically along the c axis with a slight canting toward the a axis. The Er^{3+} spins are paramagnetic and directed to the a axis by the weak Fe^{3+} magnetization. (b) In the low-temperature ($T < T_c$, Γ_{12}) phase, the Er^{3+} spins are ordered antiferromagnetically along the c axis, and the AFM vector $\mathbf{S}^A - \mathbf{S}^B$ of the Fe^{3+} spins rotates in the bc plane.

A theoretical model for describing the LTPT was proposed by Vitebskii and Yablonskii in 1978 [45]. The ratio between the Er^{3+} – Er^{3+} and Er^{3+} – Fe^{3+} interaction strengths was theoretically investigated by Kadomtseva, Krynetskii, and Matveev in 1980 [46]. They also mentioned the analogy between the LTPT and the cooperative Jahn–Teller transition [47, 48]. The analogy between the cooperative Jahn–Teller transition and the SRPT was discussed by Loos in 1984 [49] and also by Larson in 2008 [50]. Loos also suggested a magnetic system consisting of coupled ferromagnetic and paramagnetic spins, such as rare-earth iron garnets, as a candidate system for observing the above analogy. However, this analogy has not yet been verified experimentally.

ErFeO_3 can be modeled as coupled antiferromagnetic and paramagnetic (or antiferromagnetic) spins. In the above-mentioned studies, unfortunately, the analogy between the LTPT and the SRPT was not directly drawn either theoretically or experimentally. In 2018, the \sqrt{N} -dependence (N is the Er^{3+} density) of the anticrossing frequency, or vacuum Rabi splitting ($2g$), between paramagnetic Er^{3+} spins and a Fe^{3+} magnon mode was confirmed experimentally at $T > T_c$ by Li *et al* [33]. This \sqrt{N} -dependence, the Dicke cooperativity, can be taken as evidence that the coupling between the Er^{3+} spin ensemble and the Fe^{3+} magnon mode is cooperative, well described by the Dicke model or its extension.

As pointed out in the early studies [45, 46], it is important to take into account not only the Er^{3+} –magnon coupling but also the antiferromagnetic Er^{3+} – Er^{3+} exchange interactions for discussing the LTPT in ErFeO_3 . Therefore, we must extend the Dicke model to fully describe the LTPT, because Eq. (1) does not include the atom–atom interactions that correspond to the Er^{3+} – Er^{3+} exchange interactions. In our experiments [33], while the Er^{3+} –magnon coupling was clearly observed through terahertz

absorption spectroscopy, the influence of the Er^{3+} - Er^{3+} interactions remained unclear.

We determined the parameters in our spin model (Sec. IV), including the Er^{3+} - Er^{3+} interactions, through terahertz spectra that we observed previously [33] as well as the phase diagrams obtained in a recent magnetization study [34]. The parameter estimation method is discussed in Appendices, and we focus on the analogy between the LTPT and SRPT in the following sections.

IV. SPIN MODEL

Each unit cell of ErFeO_3 contains four Er^{3+} ions and four Fe^{3+} ions. The four Fe^{3+} spins, each of which has an angular momentum of $\hbar S = (5/2)\hbar$, are oriented in different directions with each other even in the absence of an external DC magnetic field [51]. However, it is known that the Fe^{3+} spin resonances (magnon modes) are well described by considering only two spins $\hat{S}^{A/B}$, each of which in fact consists of two real Fe^{3+} spins but is usually treated as a single spin with $S = 5/2$. In such a two-sublattice model of Fe^{3+} , as depicted in Fig. 1(a), at $T_c < T \lesssim 90$ K, the two spins $\hat{S}^{A/B}$ are ordered antiferromagnetically along the c axis, while they are slightly canted toward the a axis and show a weak magnetization (the Fe^{3+} spins show the so-called spin-reorientation transition at $90 \text{ K} \lesssim T \lesssim 100 \text{ K}$ [34, 43, 44]). On the other hand, Er^{3+} spins are paramagnetic at $T > T_c$, and they are directed along the a axis by the weak Fe^{3+} magnetization. This phase is called the Γ_2 phase [46].

At $T < T_c$, as shown in Fig. 1(b), when we use a two-sublattice model also for Er^{3+} spins, they are ordered antiferromagnetically along the c axis, with a canting toward the a axis due to the Fe^{3+} magnetization. Simultaneously, the Fe^{3+} AFM vector gradually rotates in the bc plane. The rotation angle measured from the c axis, φ , has been estimated to be 49° at $T = 0 \text{ K}$ [46]. This low-temperature phase is called the Γ_{12} phase [46].

In the following, we describe our spin model for $\text{Er}_x\text{Y}_{1-x}\text{FeO}_3$ ($0 \leq x \leq 1$), which is consistent with our previous experimental study [33]. The x -dependence is described in more detail in Appendix C. The replacement of Er^{3+} ions by non-magnetic Y^{3+} ones simply reduces the density of the rare-earth (Er^{3+}) spins without changing the crystal structure or the magnetic configuration of Fe^{3+} spins in the Γ_2 phase [33, 52].

Our Hamiltonian for the spins in $\text{Er}_x\text{Y}_{1-x}\text{FeO}_3$ consists of three parts:

$$\mathcal{H} = \mathcal{H}_{\text{Fe}} + \mathcal{H}_{\text{Er}} + \mathcal{H}_{\text{Fe-Er}}, \quad (7)$$

where \mathcal{H}_{Fe} , \mathcal{H}_{Er} , and $\mathcal{H}_{\text{Fe-Er}}$ are the Hamiltonians of the Fe^{3+} spins, Er^{3+} spins, and Er^{3+} - Fe^{3+} interactions, respectively.

As explained above, we employ the two-sublattice model for Fe^{3+} spins by following Herrmann's model [53] and our previous studies [33, 54]. The Hamiltonian of

Fe^{3+} spins is described as

$$\begin{aligned} \hat{\mathcal{H}}_{\text{Fe}} = & \sum_{s=A,B} \sum_{i=1}^{N_0} \mu_B \hat{S}_i^s \cdot \mathbf{g}^{\text{Fe}} \cdot \mathbf{B}^{\text{DC}} + J_{\text{Fe}} \sum_{\text{n.n.}} \hat{S}_i^A \cdot \hat{S}_{i'}^B \\ & - D_y^{\text{Fe}} \sum_{\text{n.n.}} \left(\hat{S}_{i,z}^A \hat{S}_{i',x}^B - \hat{S}_{i',z}^B \hat{S}_{i,x}^A \right) \\ & - \sum_{i=1}^{N_0} \left(A_x \hat{S}_{i,x}^A{}^2 + A_z \hat{S}_{i,z}^A{}^2 + A_{xz} \hat{S}_{i,x}^A \hat{S}_{i,z}^A \right) \\ & - \sum_{i=1}^{N_0} \left(A_x \hat{S}_{i,x}^B{}^2 + A_z \hat{S}_{i,z}^B{}^2 - A_{xz} \hat{S}_{i,x}^B \hat{S}_{i,z}^B \right). \quad (8) \end{aligned}$$

Here, $\hat{S}_i^{A/B}$ is the operator of the Fe^{3+} spin with $S = 5/2$ at the i -th site in the A/B sublattice. $\sum_{\text{n.n.}}$ means a summation over all the nearest neighbor couplings. The number of nearest neighbors is

$$z_{\text{Fe}} = 6. \quad (9)$$

N_0 is the number of Fe^{3+} spins in each sublattice and is equal to the number of unit cells in ErFeO_3 . Then, there are in total $2N_0$ spins representing the Fe^{3+} subsystem. μ_B is the Bohr magneton, and

$$\mathbf{g}^{\text{Fe}} \equiv \begin{pmatrix} g_x^{\text{Fe}} & 0 & 0 \\ 0 & g_y^{\text{Fe}} & 0 \\ 0 & 0 & g_z^{\text{Fe}} \end{pmatrix} \quad (10)$$

is the g -factor tensor for the Fe^{3+} spins. In the following, the g -factor of free electron spin is expressed as \mathbf{g} . \mathbf{B}^{DC} is an external DC magnetic flux density. J_{Fe} and D_y^{Fe} are, respectively, the strengths of isotropic and Dzyaloshinskii-Moriya-type exchange interaction strengths between Fe^{3+} spins. A_x , A_z , and A_{xz} are the energies expressing the magnetic anisotropy of Fe^{3+} spins.

While we expressed the Er^{3+} subsystem by a single spin lattice for the paramagnetic Er^{3+} spins ($T > T_c$) in our previous studies [33, 54], we use a two-sublattice model for Er^{3+} spins in this paper in order to describe the Er^{3+} - Er^{3+} exchange interaction and the LTPT. The Hamiltonian of Er^{3+} spins is expressed as

$$\hat{\mathcal{H}}_{\text{Er}} = - \sum_{s=A,B} \sum_{i=1}^{N_0} \hat{\mu}_i^s \cdot \mathbf{B}^{\text{DC}} + J_{\text{Er}} \sum_{\text{n.n.}} \hat{R}_i^A \cdot \hat{R}_{i'}^B. \quad (11)$$

Here, $\hat{R}_i^{A/B}$ is the operator of rare-earth (Er^{3+} or Y^{3+}) spin at the i -site in the A/B sublattice. For $\text{Er}_x\text{Y}_{1-x}\text{FeO}_3$, the rare-earth spins are represented randomly as ($s = A, B$)

$$\hat{R}_i^s = \begin{cases} \hat{\sigma}_i^s & \text{for } \text{Er}^{3+} \\ \mathbf{0} & \text{for } \text{Y}^{3+} \end{cases} \quad (12)$$

We describe each Er^{3+} spin by a Pauli operator $\hat{\sigma}_i^s$. The Y^{3+} ion is nonmagnetic and \hat{R}_i^s is replaced by $\mathbf{0}$. The

first term in Eq. (11) represents the Zeeman effect, and the magnetic moment is expressed in terms of anisotropic g -factors, $\mathbf{g}_{x,y,z}^{\text{Er}}$, for the Er^{3+} spins as

$$\hat{\boldsymbol{\mu}}_i^s \equiv -\frac{1}{2}\mu_B(\mathbf{g}_x^{\text{Er}} \hat{R}_{i,x}^s, \mathbf{g}_y^{\text{Er}} \hat{R}_{i,y}^s, \mathbf{g}_z^{\text{Er}} \hat{R}_{i,z}^s)^t = -\frac{1}{2}\mu_B \mathbf{g}^{\text{Er}} \cdot \hat{\mathbf{R}}_i^s. \quad (13)$$

The factor 1/2 is added since $(1/2)\hat{\boldsymbol{\sigma}}_i^s$ corresponds to a spin- $\frac{1}{2}$ operator theoretically. We defined the g -factor tensor for Er^{3+} spins as

$$\mathbf{g}^{\text{Er}} \equiv \begin{pmatrix} \mathbf{g}_x^{\text{Er}} & 0 & 0 \\ 0 & \mathbf{g}_y^{\text{Er}} & 0 \\ 0 & 0 & \mathbf{g}_z^{\text{Er}} \end{pmatrix}. \quad (14)$$

The second term in Eq. (11) represents the Er^{3+} - Er^{3+} exchange interaction with a strength of J_{Er} . Since Er^{3+} ions are diluted in $\text{Er}_x\text{Y}_{1-x}\text{FeO}_3$, the number of nearest neighbor Er^{3+} spins is effectively given by

$$z_{\text{Er}} = 6x. \quad (15)$$

In a similar manner to our previous studies [33, 54], we describe the Er^{3+} - Fe^{3+} interaction Hamiltonian as

$$\hat{\mathcal{H}}_{\text{Er-Fe}} = \sum_{i=1}^{N_0} \sum_{s,s'=A,B} \left[J \hat{\mathbf{R}}_i^s \cdot \hat{\mathbf{S}}_i^{s'} + \mathbf{D}^{s,s'} \cdot (\hat{\mathbf{R}}_i^s \times \hat{\mathbf{S}}_i^{s'}) \right]. \quad (16)$$

In our model, the Er^{3+} - Fe^{3+} interaction is closed in each unit cell, i.e., the Er^{3+} and Fe^{3+} spins in the same unit cell interact with each other but do not interact with the spins in other unit cells. J and $\mathbf{D}^{s,s'}$ are the strengths of the isotropic and antisymmetric exchange interactions, respectively. Considering the spin configuration at $T < T_c$ with no external DC magnetic field (see more details in Appendix B), we assume that $\mathbf{D}^{s,s'}$ are expressed in terms of two values D_x and D_y as

$$\mathbf{D}^{\text{A,A}} = (D_x, D_y, 0)^t, \quad (17a)$$

$$\mathbf{D}^{\text{A,B}} = (-D_x, -D_y, 0)^t, \quad (17b)$$

$$\mathbf{D}^{\text{B,A}} = (-D_x, D_y, 0)^t, \quad (17c)$$

$$\mathbf{D}^{\text{B,B}} = (D_x, -D_y, 0)^t. \quad (17d)$$

Note that, as explained in Appendix A, we assume that the y components, $\hat{R}_{i,y}^{\text{A/B}}$, of the Er^{3+} spins are not influenced by the Er^{3+} - Fe^{3+} interaction by implicitly considering a higher energy potential than the Er^{3+} - Fe^{3+} interaction strengths J and $\mathbf{D}^{s,s'}$ along the b axis. This assumption is required for properly describing the LTPT.

The actual values of the parameters that appears in our spin model are shown in Appendix D, together with a description of how we determined them.

V. PHASE DIAGRAMS

In this section, we show thermal-equilibrium (averaged) values of the Er^{3+} spins $\bar{\boldsymbol{\sigma}}^{\text{A/B}}$ and of the Fe^{3+}

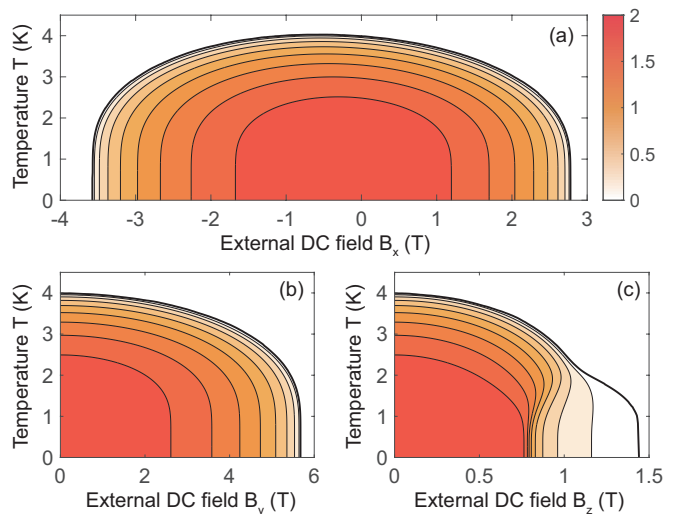


FIG. 2. Phase diagrams of spins in ErFeO_3 calculated by the mean-field method. An external DC magnetic field is applied along the (a) a , (b) b , and (c) c axes, respectively. The difference $|\bar{\sigma}_z^{\text{A}} - \bar{\sigma}_z^{\text{B}}|$ of the z components of the thermal-equilibrium values of Er^{3+} spins is mapped with red color. The bold solid lines represent the phase boundaries. The external DC magnetic field is varied from zero to positive or negative values at a fixed temperature. Since ErFeO_3 shows a weak magnetization along the a axis, the critical field depends on whether the field is parallel or antiparallel to the magnetization in Fig. 2(a).

spins $\bar{\mathbf{S}}^{\text{A/B}}$ in the zero-wavenumber (infinite-wavelength) limit by a mean-field method. Details of the mean-field method are given in Appendix A. Since we simply consider a homogeneous external DC magnetic flux density, \mathbf{B}^{DC} , in this paper, $\bar{\boldsymbol{\sigma}}^{\text{A/B}}$ and $\bar{\mathbf{S}}^{\text{A/B}}$ are independent of the site index i .

Figures 2(a), (b), and (c) show calculated phase diagrams as a function of temperature, T , and external DC magnetic flux density, \mathbf{B}^{DC} , applied along the a , b , and c axes, respectively. We plot the difference $|\bar{\sigma}_z^{\text{A}} - \bar{\sigma}_z^{\text{B}}|$ of the z components of the thermal-equilibrium values of Er^{3+} spins (AFM vector) with red color. It is the order parameter for the LTPT in the presence of an external DC magnetic field in general, while the rotation angle of the Fe^{3+} AFM vector can be an alternative order parameter if the external DC field is zero or along the a axis. The bold solid lines represent the phase boundaries. These phase diagrams well reproduce those observed by Zhang *et al.* [34]. As shown in Fig. 2(a), since ErFeO_3 possesses a weak magnetization along the a axis, the critical field depends on whether the field is parallel or antiparallel to the magnetization. The parameters used in the calculation are shown in Appendix D.

In Fig. 3, we plot the thermal-equilibrium values of the Er^{3+} and Fe^{3+} spins in the absence of an external DC magnetic field as a function of temperature. The LTPT, i.e., the antiferromagnetic ordering of Er^{3+} spins along the c axis and the rotation of the Fe^{3+} spins in

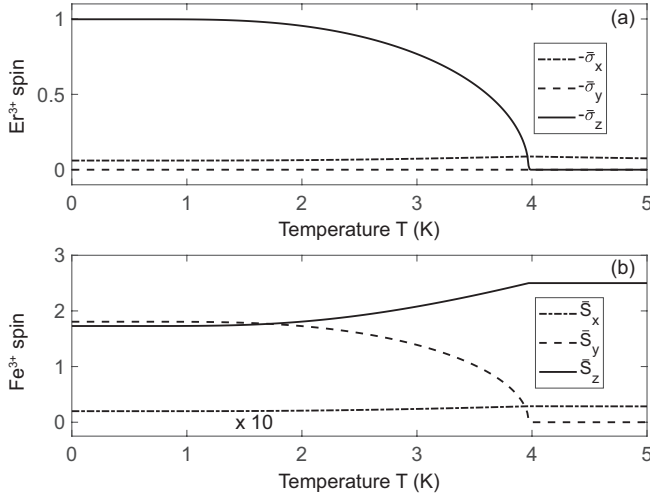


FIG. 3. The thermal-equilibrium values of (a) Er^{3+} spin and (b) Fe^{3+} spin calculated by the mean-field method are plotted as a function of temperature T in the case of zero external DC magnetic field. As shown in Fig. 3(a), $\bar{\sigma}_z = \bar{\sigma}_z^A = -\bar{\sigma}_z^B$ spontaneously appears below the critical temperature $T_c = 4.0$ K, i.e., the Er^{3+} spins are antiferromagnetically ordered along the c axis. They show a magnetization along the a axis as $\bar{\sigma}_x = \bar{\sigma}_x^{A/B}$ due to the Er^{3+} - Fe^{3+} exchange interaction with the weak Fe^{3+} magnetization along the a axis, while $\bar{\sigma}_y = \bar{\sigma}_y^{A/B} = 0$. As shown in Fig. 3(b), above T_c , the Fe^{3+} spins are ordered antiferromagnetically along the c axis as $\bar{S}_z = -\bar{S}_z^A = \bar{S}_z^B$, while they are slightly canted toward the a axis as $\bar{S}_x = \bar{S}_x^{A/B}$, and $\bar{S}_y = \bar{S}_y^A = -\bar{S}_y^B = 0$. Below T_c , the Fe^{3+} spins rotate in the bc plane, and the rotation angle is $\varphi = \arctan(\bar{S}_y/\bar{S}_z) = 46^\circ$ at $T = 0$ K with our parameters.

the bc plane [46] are well reproduced in our spin model. The rotation angle of the Fe^{3+} AFM vector is $\varphi = 46^\circ$ at $T = 0$ K with our parameters. This is approximately equal to the experimentally estimated value $\varphi = 49^\circ$ [46].

VI. EXTENDED DICKE HAMILTONIAN

In the previous sections, we discussed the LTPT of ErFeO_3 through mean-field calculations based on our spin model. It is a standard approach for analyzing magnetic phase transitions. In this section, in order to discuss the analogy between the LTPT and the SRPT in the Dicke model, we transform the spin model, Eq. (7), into an extended version of the Dicke model, including direct Er^{3+} - Er^{3+} exchange interactions, which were not considered in our previous studies [33, 54].

We first rewrite the Fe^{3+} subsystem in terms of the annihilation and creation operators of a magnon in Sec. VI A. The Er^{3+} subsystem is rewritten by large spin operators in Sec. VI B. The Er^{3+} - Fe^{3+} exchange interactions are transformed into five Er^{3+} -magnon couplings in Sec. VI C. The total Hamiltonian is given in Sec. VI D.

A. Fe^{3+} subsystem

We assume that the most-stable values of the Fe^{3+} spins at zero temperature, $\bar{\mathbf{S}}^{A/B}$, are unchanged when an external DC magnetic flux density \mathbf{B}^{DC} ($\lesssim 10$ T) is applied, as we also assumed in our previous studies [33, 54]. Under this assumption, as depicted in Fig. 1(a), the most stable state (i.e., ground state) of the Fe^{3+} subsystem $\hat{\mathcal{H}}_{\text{Fe}}$, Eq. (8), are expressed as

$$\bar{\mathbf{S}}_0^A = \begin{pmatrix} S \sin \beta_0 \\ 0 \\ -S \cos \beta_0 \end{pmatrix}, \quad \bar{\mathbf{S}}_0^B = \begin{pmatrix} S \sin \beta_0 \\ 0 \\ S \cos \beta_0 \end{pmatrix}. \quad (18)$$

Here, the canting angle β_0 is expressed as (see Appendix E or Refs. 33, 53, and 54)

$$\beta_0 = -\frac{1}{2} \arctan \frac{A_{xy} + z_{\text{Fe}} D_y^{\text{Fe}}}{z_{\text{Fe}} J_{\text{Fe}} - A_x + A_z}. \quad (19)$$

The magnon is the quantum of spin fluctuations from this stable state. As shown in Appendix E as well as in Refs. 33 and 54, in the long wavelength limit, the Fe^{3+} Hamiltonian $\hat{\mathcal{H}}_{\text{Fe}}$, Eq. (8), can be rewritten in terms of the annihilation (creation) operators \hat{a}_K (\hat{a}_K^\dagger) of Fe^{3+} magnons as

$$\hat{\mathcal{H}}_{\text{Fe}} \approx \sum_{K=0,\pi} \hbar \omega_K \hat{a}_K^\dagger \hat{a}_K + \text{const.} \quad (20)$$

Here, $K = 0$ and π correspond to the quasi-ferromagnetic (qFM) and quasi-antiferromagnetic (qAFM) magnon modes [53], respectively. Their eigenfrequencies can be obtained as

$$\omega_K = \gamma \sqrt{(b \cos K - a)(d \cos K + c)}, \quad (21)$$

where we defined

$$a = [S/(\mathbf{g}\mu_B)][-A_z - A_x - (z_{\text{Fe}} J_{\text{Fe}} + A_z - A_x) \cos(2\beta_0) + (A_{xz} + z_{\text{Fe}} D_y^{\text{Fe}}) \sin(2\beta_0)], \quad (22a)$$

$$b = [S/(\mathbf{g}\mu_B)](z_{\text{Fe}} J_{\text{Fe}}), \quad (22b)$$

$$c = [S/(\mathbf{g}\mu_B)][(z_{\text{Fe}} J_{\text{Fe}} + 2A_z - 2A_x) \cos(2\beta_0) + z_{\text{Fe}} D_y^{\text{Fe}} \sin(2\beta_0)], \quad (22c)$$

$$d = [S/(\mathbf{g}\mu_B)][-z_{\text{Fe}} J_{\text{Fe}} \cos(2\beta_0) - (2A_{xz} + z_{\text{Fe}} D_y^{\text{Fe}}) \sin(2\beta_0)]. \quad (22d)$$

The operators of the spin fluctuations $\delta \hat{\mathbf{S}}_i^{A/B} \equiv \hat{\mathbf{S}}_i^{A/B} - \bar{\mathbf{S}}_0^{A/B}$ are expressed as

$$\delta \hat{\mathbf{S}}_i^A = \sqrt{\frac{S}{2N_0}} \begin{pmatrix} -(\hat{T}_0 - \hat{T}_\pi) \cos \beta_0 \\ (\hat{Y}_0 - \hat{Y}_\pi) \\ -(\hat{T}_0 + \hat{T}_\pi) \sin \beta_0 \end{pmatrix}, \quad (23a)$$

$$\delta \hat{\mathbf{S}}_i^B = \sqrt{\frac{S}{2N_0}} \begin{pmatrix} (\hat{T}_0 + \hat{T}_\pi) \cos \beta_0 \\ (\hat{Y}_0 + \hat{Y}_\pi) \\ -(\hat{T}_0 - \hat{T}_\pi) \sin \beta_0 \end{pmatrix}, \quad (23b)$$

where we defined

$$\hat{T}_K \equiv \left(\frac{b \cos K - a}{d \cos K + c} \right)^{1/4} \frac{(\hat{a}_{-K}^\dagger + \hat{a}_K)}{\sqrt{2}}, \quad (24a)$$

$$\hat{Y}_K \equiv \left(\frac{d \cos K + c}{b \cos K - a} \right)^{1/4} \frac{i(\hat{a}_{-K}^\dagger - \hat{a}_K)}{\sqrt{2}}. \quad (24b)$$

For the discussion in the next subsections, we define the sum and difference of the spins as

$$\hat{S}_i^\pm \equiv \hat{S}_i^A \pm \hat{S}_i^B. \quad (25)$$

Their equilibrium (most stable) values are

$$\bar{S}_0^+ \equiv \bar{S}_0^A + \bar{S}_0^B = (2S \sin \beta_0, 0, 0)^t, \quad (26a)$$

$$\bar{S}_0^- \equiv \bar{S}_0^A - \bar{S}_0^B = (0, 0, -2S \cos \beta_0)^t, \quad (26b)$$

and their fluctuations are expressed as

$$\delta \hat{S}^+ \equiv \delta \hat{S}_i^A + \delta \hat{S}_i^B = \sqrt{\frac{2S}{N_0}} \begin{pmatrix} \hat{T}_\pi \cos \beta_0 \\ \hat{Y}_0 \\ -\hat{T}_0 \sin \beta_0 \end{pmatrix}, \quad (27a)$$

$$\delta \hat{S}^- \equiv \delta \hat{S}_i^A - \delta \hat{S}_i^B = \sqrt{\frac{2S}{N_0}} \begin{pmatrix} -\hat{T}_0 \cos \beta_0 \\ -\hat{Y}_\pi \\ \hat{T}_\pi \sin \beta_0 \end{pmatrix}. \quad (27b)$$

B. Er³⁺ subsystem

We define following new operators:

$$\hat{\Sigma}^{A/B} \equiv \frac{1}{2} \sum_{i=1}^{N_0} \hat{R}_i^{A/B}. \quad (28)$$

For an Er³⁺ ion, $(1/2)\hat{R}_i^{A/B}$ is a spin- $\frac{1}{2}$ operator. The total number of spin- $\frac{1}{2}$ spins (Er³⁺ spins) in the two sublattices is

$$N \equiv 2xN_0. \quad (29)$$

Then, $\hat{\Sigma}^{A/B}$ is a spin- $\frac{N}{4}$ operator representing the rare-earth spins in the A/B sublattice. We also define the sum and difference of the two sublattice spins as

$$\hat{\Sigma}^\pm \equiv \hat{\Sigma}^A \pm \hat{\Sigma}^B. \quad (30)$$

In the long-wavelength limit, all the spins in each sublattice have the same values in both static and dynamical situations. Then, the Er³⁺ Hamiltonian in Eq. (11) can be rewritten as

$$\begin{aligned} \hat{H}_{\text{Er}} & \\ & \approx \sum_{\xi=x,y,z} \mathfrak{g}_\xi^{\text{Er}} \mu_B \hat{\Sigma}_\xi^+ B_\xi^{\text{DC}} + z_{\text{Er}} J_{\text{Er}} \sum_{i=1}^{N_0} \hat{R}_i^A \cdot \sum_{i'=1}^{N_0} \frac{\hat{R}_{i'}^B}{xN_0} \end{aligned} \quad (31a)$$

$$= \sum_{\xi=x,y,z} \mathfrak{g}_\xi^{\text{Er}} \mu_B \hat{\Sigma}_\xi^+ B_\xi^{\text{DC}} + \frac{8z_{\text{Er}} J_{\text{Er}}}{N} \hat{\Sigma}^A \cdot \hat{\Sigma}^B. \quad (31b)$$

C. Er³⁺-Fe³⁺ interactions

In the same manner as in Refs. 33 and 54, we rewrite the Hamiltonian of the Er³⁺-Fe³⁺ exchange interactions, Eq. (16), as

$$\begin{aligned} \hat{H}_{\text{Er-Fe}} & \approx 2J \left(\hat{\Sigma}^+ \cdot \bar{S}_0^+ + \hat{\Sigma}^+ \cdot \delta \hat{S}^+ \right) \\ & + \begin{pmatrix} 0 \\ 2D_y \\ 0 \end{pmatrix} \cdot \left(\hat{\Sigma}^+ \times \bar{S}_0^- + \hat{\Sigma}^+ \times \delta \hat{S}^- \right) \\ & + \begin{pmatrix} 2D_x \\ 0 \\ 0 \end{pmatrix} \cdot \left(\hat{\Sigma}^- \times \bar{S}_0^- + \hat{\Sigma}^- \times \delta \hat{S}^- \right). \end{aligned} \quad (32)$$

In each parenthesis, the first terms represent the influence of the static components (equilibrium values) $\bar{S}_0^{A/B}$ of Fe³⁺ spins to Er³⁺ spins $\hat{\Sigma}^\pm$, and the second terms represent the coupling between the Fe³⁺ fluctuation $\delta \hat{S}^\pm$ and the Er³⁺ spins $\hat{\Sigma}^\pm$. We divide these terms into the two Hamiltonians as

$$\hat{H}_{\text{Er-Fe}} = \hat{H}_{\text{Er-Fe}}^\Sigma + \hat{H}_{\text{Er-Fe}}^{\text{coupling}}. \quad (33)$$

The first term gives a part of the Er³⁺ spin resonance frequency, and it is expressed as

$$\hat{H}_{\text{Er-Fe}}^\Sigma = E_x \hat{\Sigma}_x^+, \quad (34)$$

where we used Eqs. (26) and E_x is defined as

$$E_x \equiv 4S(J \sin \beta_0 + D_y \cos \beta_0). \quad (35)$$

Note that we neglected $(-4SD_x \cos \beta_0) \hat{\Sigma}_y^-$ under the assumption explained at the end of Sec. IV. The second term in Eq. (33) is rewritten in terms of the Fe³⁺ fluctuations as

$$\begin{aligned} \hat{H}_{\text{Er-Fe}}^{\text{coupling}} & = \sqrt{\frac{8S}{N_0}} \left[(J \cos \beta_0 - D_y \sin \beta_0) \hat{T}_\pi \hat{\Sigma}_x^+ \right. \\ & + J \hat{Y}_0 \hat{\Sigma}_y^+ + (D_x \sin \beta_0) \hat{T}_\pi \hat{\Sigma}_y^- + D_x \hat{Y}_\pi \hat{\Sigma}_z^- \\ & \left. + (-J \sin \beta_0 - D_y \cos \beta_0) \hat{T}_0 \hat{\Sigma}_z^+ \right]. \end{aligned} \quad (36)$$

D. Total system

The total Hamiltonian derived from our spin model is finally expressed as

$$\begin{aligned} \hat{H} & \approx \sum_{K=0,\pi} \hbar \omega_K \hat{a}_K^\dagger \hat{a}_K + E_x \hat{\Sigma}_x^+ + \sum_{\xi=x,y,z} \mathfrak{g}_\xi^{\text{Er}} \mu_B B_\xi^{\text{DC}} \hat{\Sigma}_\xi^+ \\ & + \frac{8z_{\text{Er}} J_{\text{Er}}}{N} \hat{\Sigma}^A \cdot \hat{\Sigma}^B + \frac{2\hbar g_x}{\sqrt{N}} (\hat{a}_\pi^\dagger + \hat{a}_\pi) \hat{\Sigma}_x^+ \\ & + \frac{i2\hbar g_y}{\sqrt{N}} (\hat{a}_0^\dagger - \hat{a}_0) \hat{\Sigma}_y^+ + \frac{2\hbar g_y'}{\sqrt{N}} (\hat{a}_\pi^\dagger + \hat{a}_\pi) \hat{\Sigma}_y^- \\ & + \frac{i2\hbar g_z}{\sqrt{N}} (\hat{a}_\pi^\dagger - \hat{a}_\pi) \hat{\Sigma}_z^- + \frac{2\hbar g_z'}{\sqrt{N}} (\hat{a}_0^\dagger + \hat{a}_0) \hat{\Sigma}_z^+. \end{aligned} \quad (37)$$

Here, the five Er^{3+} -magnon coupling terms in Eq. (36) were rewritten in terms of the annihilation (creation) operators \hat{a}_K (\hat{a}_K^\dagger) of a magnon. The five coupling strengths are defined as

$$\begin{aligned} \hbar g_x &= \sqrt{2xS}(J \cos \beta_0 - D_y \sin \beta_0) \left(\frac{b+a}{d-c} \right)^{1/4} \\ &= h \times \sqrt{x} \times 0.051 \text{ THz}, \end{aligned} \quad (38a)$$

$$\begin{aligned} \hbar g_y &= \sqrt{2xS}J \left(\frac{d+c}{b-a} \right)^{1/4} \\ &= h \times \sqrt{x} \times 0.041 \text{ THz}, \end{aligned} \quad (38b)$$

$$\begin{aligned} \hbar g'_y &= \sqrt{2xS}(D_x \sin \beta_0) \left(\frac{b+a}{d-c} \right)^{1/4} \\ &= h \times \sqrt{x} \times 3.1 \times 10^{-5} \text{ THz}, \end{aligned} \quad (38c)$$

$$\begin{aligned} \hbar g_z &= \sqrt{2xS}D_x \left(\frac{d-c}{b+a} \right)^{1/4} \\ &= h \times \sqrt{x} \times 0.116 \text{ THz}, \end{aligned} \quad (38d)$$

$$\begin{aligned} \hbar g'_z &= \sqrt{2xS}(-J \sin \beta_0 - D_y \cos \beta_0) \left(\frac{b-a}{d+c} \right)^{1/4} \\ &= h \times \sqrt{x} \times (-0.040 \text{ THz}). \end{aligned} \quad (38e)$$

The actual values are evaluated by the parameters shown in Appendix D. Note that, compared with the expression in our previous studies [33, 54], the above coupling strengths have additional factors: $\sqrt{2}$ and \sqrt{S} . The first of these factors, $\sqrt{2}$, originates from the number of Er^{3+} sublattices in the present study, while a single Er^{3+} lattice was considered in our previous studies [33, 54]. On the other hand, the second factor, \sqrt{S} , comes from the difference in the way of normalizing the Fe^{3+} spins between the present and previous studies [33, 54].

VII. ANALOGY BETWEEN THE TWO PHASE TRANSITIONS

Based on the extended Dicke Hamiltonian, Eq. (37), derived in the previous section, we show in this section that the LTPT in ErFeO_3 is a magnonic SRPT.

In Sec. VII A, we show that the Er^{3+} -qAFM magnon coupling with a strength of g_z corresponds to the matter-photon coupling in the SRPT case. We also demonstrate that the thermal SRPT predicted by the extended Dicke Hamiltonian correctly reproduces the temperature-dependence of the Er^{3+} and Fe^{3+} spins shown in Fig. 3. In Sec. VII B, we quantitatively compare the contributions of the Er^{3+} -magnon coupling and the Er^{3+} - Er^{3+} exchange interactions in the LTPT. We show that the LTPT can be caused solely by the Er^{3+} -magnon coupling. Furthermore, we demonstrate that the Er^{3+} -magnon coupling enhances the critical temperature and critical magnetic field of the phase transition, compared with the case in which the phase transition is driven by the Er^{3+} - Er^{3+} exchange interactions alone.

A. Correspondence

In this section, by using the semiclassical method described in Sec. II with the extended Dicke Hamiltonian, Eq. (37), we calculate the thermal-equilibrium values of Er^{3+} and Fe^{3+} spins and magnon amplitudes as a function of temperature.

While the Er^{3+} spin ensemble is described by six operators, $\hat{\Sigma}_{x,y,z}^+$ and $\hat{\Sigma}_{x,y,z}^-$, in the extended Dicke Hamiltonian, only $\hat{\Sigma}_x^+$ and $\hat{\Sigma}_z^-$ are relevant to the LTPT depicted in Fig. 1. $\hat{\Sigma}_x^+$ corresponds to the paramagnetic alignment by the Fe^{3+} magnetization along the a axis, and $\hat{\Sigma}_z^-$ corresponds to the antiferromagnetic ordering along the c axis. Then, for analyzing the thermal-equilibrium values of the spins, we need to consider only the following two terms in the Er^{3+} - Er^{3+} exchange interactions:

$$\begin{aligned} \frac{8z_{\text{Er}}J_{\text{Er}}}{N} \hat{\Sigma}^A \cdot \hat{\Sigma}^B &= \frac{2z_{\text{Er}}J_{\text{Er}}}{N} \sum_{\xi=x,y,z} \left[(\hat{\Sigma}_\xi^+)^2 - (\hat{\Sigma}_\xi^-)^2 \right] \\ &\rightarrow \frac{2z_{\text{Er}}J_{\text{Er}}}{N} \left[(\hat{\Sigma}_x^+)^2 - (\hat{\Sigma}_z^-)^2 \right]. \end{aligned} \quad (39)$$

On the other hand, while Fe^{3+} spins are described by the qFM and qAFM magnon modes in the extended Dicke Hamiltonian, only the qAFM mode is relevant to the LTPT. As shown in Fig. 1, $\delta\hat{S}_y^-$ and $\delta\hat{S}_z^-$ are required for describing the rotation of the Fe^{3+} AFM vector in the bc plane, and $\delta\hat{S}_x^+$ is required for the possible modulation of canting along the a axis. As seen in Eqs. (27), they are related to the qAFM magnon mode ($K = \pi$), and the qFM mode ($K = 0$) plays no role in the LTPT.

Consequently, among the terms in the total Hamiltonian given by Eq. (37), we only need to consider the following terms for describing the LTPT (the other terms are required for fully reproducing the THz spectra as discussed in Appendix C):

$$\begin{aligned} \hat{\mathcal{H}}/\hbar &\rightarrow \omega_\pi \hat{a}_\pi^\dagger \hat{a}_\pi + \omega_{\text{Er}} \hat{\Sigma}_x + \frac{2z_{\text{Er}}J_{\text{Er}}}{N\hbar} \left(\hat{\Sigma}_x^2 - \hat{\Sigma}_z^2 \right) \\ &+ \frac{2g_x}{\sqrt{N}} (\hat{a}_\pi^\dagger + \hat{a}_\pi) \hat{\Sigma}_x + \frac{i2g_z}{\sqrt{N}} (\hat{a}_\pi^\dagger - \hat{a}_\pi) \hat{\Sigma}_z. \end{aligned} \quad (40)$$

Here, the Er^{3+} resonance frequency is defined as

$$\omega_{\text{Er}} \equiv \frac{|E_x + \mathfrak{g}_x^{\text{Er}} \mu_B B_x^{\text{DC}}|}{\hbar}. \quad (41)$$

Note that we re-wrote the large spin operators representing the Er^{3+} spin ensemble as

$$\begin{cases} \hat{\Sigma}_x^+ \rightarrow \hat{\Sigma}_x \equiv \sum_{i=1}^N \hat{\sigma}_{i,x}/2 \\ \hat{\Sigma}_y^- \rightarrow \hat{\Sigma}_y \equiv \sum_{i=1}^N \hat{\sigma}_{i,y}/2 \\ \hat{\Sigma}_z^- \rightarrow \hat{\Sigma}_z \equiv \sum_{i=1}^N \hat{\sigma}_{i,z}/2 \end{cases} \quad (42)$$

where we re-indexed the Pauli operators representing the Er^{3+} spins in the two sublattices as

$$\begin{cases} \hat{\sigma}_{i,x}^A \rightarrow \hat{\sigma}_{2i-1,x} \\ \hat{\sigma}_{i,y}^A \rightarrow \hat{\sigma}_{2i-1,y} \\ \hat{\sigma}_{i,z}^A \rightarrow \hat{\sigma}_{2i-1,z} \end{cases} \quad \begin{cases} \hat{\sigma}_{i,x}^B \rightarrow \hat{\sigma}_{2i,x} \\ \hat{\sigma}_{i,y}^B \rightarrow -\hat{\sigma}_{2i,y} \\ \hat{\sigma}_{i,z}^B \rightarrow -\hat{\sigma}_{2i,z} \end{cases} \quad (43)$$

In Eq. (40), we assumed that the external DC magnetic field is applied along the a axis for keeping the Γ_{12} symmetry, where either $|\bar{\sigma}_z^A - \bar{\sigma}_z^B|$ or the rotation angle φ of the Fe^{3+} AFM vector from the c axis can be the order parameter for the LTPT. Among the five Er^{3+} -magnon couplings in Eq. (37), only the g_x and g_z terms are required for considering the coupling between $\hat{\Sigma}_{x,z}$ and the qAFM magnons. While the g_y term also couples $\hat{\Sigma}_y$ and qAFM magnons, its coupling strength is negligible compared with $g_{x,z}$, as shown in Eqs. (38), consistent with the experimentally observed antiferromagnetic ordering of Er^{3+} spins along the c axis ($\langle \hat{\Sigma}_y^- \rangle = 0$).

Through comparison of Eq. (40) with Eq. (1) (the Dicke model), we can identify the g_z term to correspond to the matter-photon coupling (transverse coupling). Additionally, the g_x term represents longitudinal coupling and the J_{Er} term describes the Er^{3+} - Er^{3+} exchange interactions in Eq. (40). The coupling strength $g_z = 2\pi \times 0.116$ THz puts the systems in the ultrastrong regime, since it is a significant fraction of the Er^{3+} resonance and qAFM magnon frequencies, $E_x = \hbar \times 0.023$ THz and $\omega_\pi = 2\pi \times 0.896$ THz. When the g_z term causes a SRPT, $\langle \hat{\Sigma}_z^- \rangle = \langle \hat{\Sigma}_z^+ \rangle$ spontaneously acquires a nonzero value in thermal equilibrium, corresponding to the antiferromagnetic ordering of Er^{3+} spins along the c axis. As will be discussed later, the spontaneous appearance of nonzero $\langle i(\hat{a}_\pi^\dagger - \hat{a}_\pi) \rangle$, which is coupled with $\hat{\Sigma}_z$ in the g_z term, corresponds to the rotation of the Fe^{3+} AFM vector.

Following the semiclassical treatment in Sec. II, we calculate the expectation values of the Er^{3+} spins and Fe^{3+} qAFM magnon operators at a finite temperature. In the thermodynamic limit, $N \rightarrow \infty$, the partition function $\mathcal{Z}(T) \equiv \text{Tr}[e^{-\hat{\mathcal{H}}/(k_B T)}]$ can be approximately evaluated by replacing the trace over the magnonic variables with an integral over c-numbers $\bar{a}_r, \bar{a}_i \in \mathbb{R}$, giving $\hat{a}_\pi \rightarrow \sqrt{N}(\bar{a}_r + i\bar{a}_i)$ as

$$\bar{\mathcal{Z}}(T) \equiv \int \frac{d\bar{a}_r d\bar{a}_i}{\pi/N} \text{Tr}[e^{-\hat{\mathcal{H}}^{\text{eff}}(\bar{a}_r, \bar{a}_i)/(k_B T)}] \quad (44a)$$

$$= \int \frac{d\bar{a}_r d\bar{a}_i}{\pi/N} e^{-\bar{\mathcal{S}}(\bar{a}, T)/(k_B T)}, \quad (44b)$$

where we defined an effective Hamiltonian

$$\begin{aligned} \hat{\mathcal{H}}^{\text{eff}}(\bar{a}_r, \bar{a}_i)/\hbar &\equiv N\omega_\pi(\bar{a}_r^2 + \bar{a}_i^2) + \omega_{\text{Er}} \hat{\Sigma}_x \\ &+ \frac{4z_{\text{Er}} J_{\text{Er}}}{N\hbar} \left(\langle \hat{\Sigma}_x \rangle \hat{\Sigma}_x - \langle \hat{\Sigma}_z \rangle \hat{\Sigma}_z \right) \\ &- \frac{2z_{\text{Er}} J_{\text{Er}}}{N\hbar} \left(\langle \hat{\Sigma}_x \rangle^2 - \langle \hat{\Sigma}_z \rangle^2 \right) \\ &+ 4g_x \bar{a}_r \hat{\Sigma}_x + 4g_z \bar{a}_i \hat{\Sigma}_z \end{aligned} \quad (45)$$

by introducing the Er^{3+} components $\langle \hat{\Sigma}_{x,z} \rangle$ of the mean-fields for the Er^{3+} ensemble. The action appearing in

Eq. (44b) is defined as

$$\begin{aligned} \bar{\mathcal{S}}(\bar{a}_r, \bar{a}_i, T) &\equiv -k_B T \ln \text{Tr}[e^{-\hat{\mathcal{H}}^{\text{eff}}(\bar{a}_r, \bar{a}_i)/(k_B T)}] \\ &= N \left\{ \hbar\omega_\pi(\bar{a}_r^2 + \bar{a}_i^2) - \frac{2z_{\text{Er}} J_{\text{Er}}}{N^2} \left(\langle \hat{\Sigma}_x \rangle^2 - \langle \hat{\Sigma}_z \rangle^2 \right) \right\} \\ &- Nk_B T \ln \text{Tr}[e^{-\hat{\mathcal{H}}^a(\bar{a}_r, \bar{a}_i)/(k_B T)}], \end{aligned} \quad (46a, 46b)$$

where we defined an effective Hamiltonian per Er^{3+} spin as

$$\begin{aligned} \frac{\hat{\mathcal{H}}^a(\bar{a}_r, \bar{a}_i)}{\hbar} &\equiv \frac{\omega_{\text{Er}}}{2} \hat{\sigma}_x + \frac{2z_{\text{Er}} J_{\text{Er}}}{N\hbar} \left(\langle \hat{\Sigma}_x^+ \rangle \hat{\sigma}_x - \langle \hat{\Sigma}_z^- \rangle \hat{\sigma}_z \right) \\ &+ 2g_x \bar{a}_r \hat{\sigma}_x + 2g_z \bar{a}_i \hat{\sigma}_z. \end{aligned} \quad (47)$$

We omitted the site index i here, since all the spins are identical. The action $\bar{\mathcal{S}}$ is minimized at $\partial \bar{\mathcal{S}}/\partial \bar{a}_r = 0$ and $\partial \bar{\mathcal{S}}/\partial \bar{a}_i = 0$, by which we get

$$\omega_\pi \bar{a}_r + g_x \langle \hat{\sigma}_x \rangle = 0, \quad (48a)$$

$$\omega_\pi \bar{a}_i + g_z \langle \hat{\sigma}_z \rangle = 0, \quad (48b)$$

where the expectation values of the Pauli operators are defined, for given \bar{a}_r and \bar{a}_i , as

$$\bar{\sigma}_\xi \equiv \langle \hat{\sigma}_\xi \rangle \equiv \frac{\text{Tr}[\hat{\sigma}_\xi e^{-\hat{\mathcal{H}}^a(\bar{a}_r, \bar{a}_i)/(k_B T)}]}{\text{Tr}[e^{-\hat{\mathcal{H}}^a(\bar{a}_r, \bar{a}_i)/(k_B T)}]}. \quad (49)$$

From Eqs. (48), the expectation values of the large spin operators are expressed as

$$\langle \hat{\Sigma}_x \rangle = \frac{N}{2} \langle \hat{\sigma}_x \rangle = -\frac{N\omega_\pi}{2g_x} \bar{a}_r, \quad (50a)$$

$$\langle \hat{\Sigma}_z \rangle = \frac{N}{2} \langle \hat{\sigma}_z \rangle = -\frac{N\omega_\pi}{2g_z} \bar{a}_i. \quad (50b)$$

Substituting these into Eq. (47), we get

$$\begin{aligned} \frac{\hat{\mathcal{H}}^a(\bar{a}_r, \bar{a}_i)}{\hbar} &= \frac{\omega_{\text{Er}}}{2} \hat{\sigma}_x + \left(2g_x - \frac{z_{\text{Er}} J_{\text{Er}} \omega_\pi}{\hbar g_x} \right) \bar{a}_r \hat{\sigma}_x \\ &+ \left(2g_z + \frac{z_{\text{Er}} J_{\text{Er}} \omega_\pi}{\hbar g_z} \right) \bar{a}_i \hat{\sigma}_z. \end{aligned} \quad (51)$$

By simultaneously solving Eqs. (48), (49), and (51) for a given temperature T , we get the thermal-equilibrium values of the Er^{3+} spins $\bar{\sigma}_{x,z}$ and Fe^{3+} qAFM magnons $\bar{a}_{r,i}$. From Eqs. (18), (23), and (24), the thermal-equilibrium values of the Fe^{3+} spins are obtained from those $\bar{a}_{r,i}$ of qAFM magnons as

$$\begin{aligned} \bar{S}_x &\equiv \langle \hat{S}_x^A \rangle = \langle \hat{S}_x^B \rangle \\ &= S \sin \beta_0 + \sqrt{2xS} \cos \beta_0 \left(\frac{b+a}{d-c} \right)^{1/4} \bar{a}_r, \end{aligned} \quad (52a)$$

$$\begin{aligned} \bar{S}_y &\equiv \langle \hat{S}_y^A \rangle = -\langle \hat{S}_y^B \rangle \\ &= -\sqrt{2xS} \left(\frac{d-c}{b+a} \right)^{1/4} \bar{a}_i, \end{aligned} \quad (52b)$$

$$\begin{aligned} \bar{S}_z &\equiv -\langle \hat{S}_z^A \rangle = \langle \hat{S}_z^B \rangle \\ &= S \cos \beta_0 - \sqrt{2xS} \sin \beta_0 \left(\frac{b+a}{d-c} \right)^{1/4} \bar{a}_r. \end{aligned} \quad (52c)$$

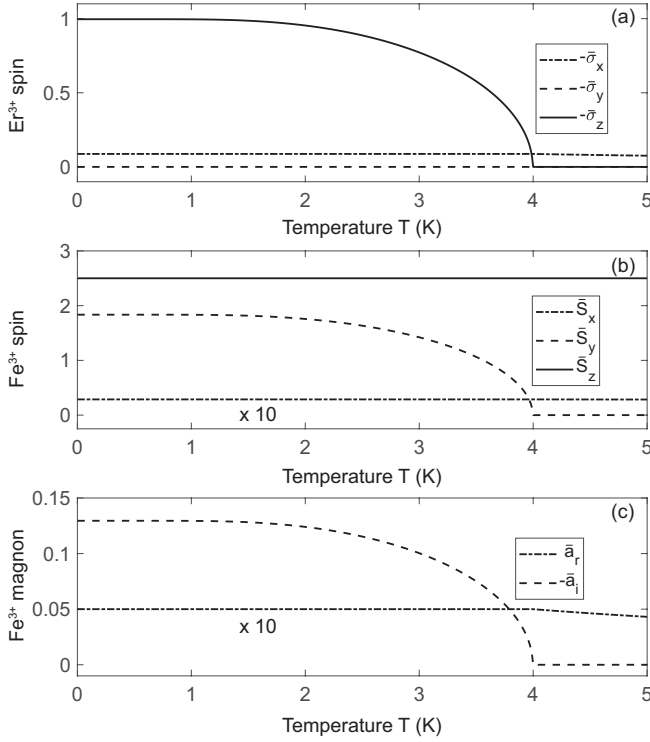


FIG. 4. Thermal-equilibrium values of (a) Er³⁺ spins, (b) Fe³⁺ spins, and (c) Fe³⁺ magnon amplitudes are plotted as a function of temperature T . They were calculated by the semiclassical method with the extended Dicke Hamiltonian in the case of zero external DC magnetic field. Figures 4(a) and (b) are almost the same as Figs. 3(a) and (b), respectively, except \bar{S}_z , which is not largely changed due to bosonization. The Fe³⁺ spins, $\bar{S}_{x,y,z}$, were calculated by Eqs. (52) with the thermal-equilibrium value of qAFM magnon annihilation operator $\langle \hat{a}_\pi \rangle = \sqrt{N}(\bar{a}_r + i\bar{a}_i)$ plotted in Fig. 4(c).

In Fig. 4, we plot the thermal-equilibrium values of (a) Er³⁺ spins, $\bar{\sigma}_{x,y,z}$, (b) Fe³⁺ spins, $\bar{S}_{x,y,z}$, and (c) Fe³⁺ qAFM magnons, $\bar{a}_{r,i}$, as a function of temperature in the absence of an external DC magnetic field, $\mathbf{B}^{\text{DC}} = \mathbf{0}$. We can see that Figs. 4(a) and (b), respectively, well reproduce Figs. 3(a) and (b) calculated by the mean-field method, including the critical temperature, T_c , but except \bar{S}_z . In Fig. 3(b), \bar{S}_z is seen to decrease, accompanied by the spontaneous appearance of \bar{S}_y , as the temperature decreases, while it is almost unchanged in Fig. 4(b). This is because $\bar{S}_x^2 + \bar{S}_y^2 + \bar{S}_z^2 = S^2$ is no longer satisfied in the extended Dicke Hamiltonian derived through magnon quantization (i.e., bosonization of Fe³⁺ spin modulations). The ultrastrong g_z term causes the spontaneous appearance of $\bar{\sigma}_z$ and \bar{a}_i , as seen in Fig. 4(a) and (c), respectively, and the latter causes the nonzero \bar{S}_y through Eq. (52b). The rotation of the Fe³⁺ AFM vector occurs in ErFeO₃ by the spontaneous appearance of nonzero \bar{S}_y when $\bar{S}_x^2 + \bar{S}_y^2 + \bar{S}_z^2 = S^2$ holds. This is the basic picture of the LTPT in terms of Er³⁺-magnon coupling.

As seen in Eqs. (38), the transverse coupling strength,

g_z , depends on D_x , and the longitudinal coupling strength, g_x , depends on J and D_y . As seen in Eq. (16), the D_x antisymmetric Er³⁺-Fe³⁺ exchange interaction is essential for the LTPT, because it couples $\hat{\sigma}_z^{A/B}$ and $\hat{S}_y^{A/B}$, which appear spontaneously at $T < T_c$. In contrast, the J and D_y exchange interactions are not directly related to the LTPT.

In this way, we can quantitatively reproduce the LTPT as the SRPT in the extended Dicke Hamiltonian, Eq. (37), which was derived from the spin model of ErFeO₃. The essential terms are extracted in Eq. (40). The g_z term (antisymmetric Er³⁺-Fe³⁺ exchange interaction with D_x) corresponds to the matter-photon coupling and causes the antiferromagnetic ordering of Er³⁺ spins along the c axis and the b component of the Fe³⁺ spins through the spontaneous appearance of qAFM magnons.

B. Er³⁺-magnon coupling contribution

Although the g_z term causes the spontaneous appearance of both $\bar{\sigma}_z$ and \bar{S}_y following the picture of the SRPT, a nonzero $\bar{\sigma}_z$ can spontaneously appear also by the J_{Er} term (Er³⁺-Er³⁺ exchange interactions). While the Er³⁺-magnon coupling is inevitable for the spontaneous rotation of Fe³⁺ AFM vector (spontaneous appearance of \bar{S}_y), we try to evaluate quantitatively the contributions of the Er³⁺-magnon coupling and Er³⁺-Er³⁺ exchange interactions for the LTPT in this subsection.

In Fig. 5, we plot the phase boundaries calculated by the full Hamiltonian (solid lines), in the absence of Er³⁺-Fe³⁺ exchange interactions (dash-dotted line; $J = D_x = D_y = g_z = g_x = 0$), and in the absence of Er³⁺-Er³⁺ exchange interactions (dashed line; $J_{\text{Er}} = 0$). Figures 5(a) and (b) show results by the mean-field method and by the semiclassical method with the extended Dicke Hamiltonian, respectively. The solid curve in Fig. 5(a) is equal to that in Fig. 2(a). The small differences between Figs. 5(a) and (b) are discussed in Appendix F.

As shown by the dashed lines ($J_{\text{Er}} = 0$), the phase transition occurs even in the absence of Er³⁺-Er³⁺ exchange interactions, and the critical temperature $T_c \sim 1.2$ K at $\mathbf{B}^{\text{DC}} = \mathbf{0}$. This means that the Er³⁺-magnon coupling alone can cause the LTPT. In this sense, the LTPT can be interpreted as a magnonic SRPT, because the Er³⁺-magnon coupling is strong enough for the phase transition to occur.

On the other hand, in the absence of Er³⁺-magnon coupling, as shown by dash-dotted lines, the critical temperature $T_c \sim 2.6$ K at $\mathbf{B}^{\text{DC}} = \mathbf{0}$. This result appears to indicate that the contribution of the Er³⁺-Er³⁺ exchange interactions is larger than that of the Er³⁺-magnon coupling. However, the real critical temperature $T_c \sim 4$ K, meaning that the Er³⁺-magnon coupling enhances the critical temperature of the phase transition. In the same manner, the critical magnetic field is also en-

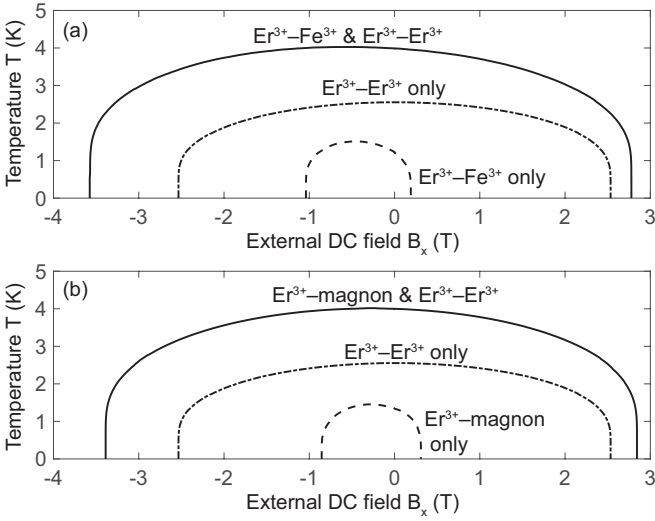


FIG. 5. Phase boundaries of the LTPT in ErFeO_3 calculated by (a) the mean-field method and (c) the semiclassical method with the extended Dicke Hamiltonian. An external DC magnetic field is applied along the a axis. The solid curves are the phase boundaries by the full Hamiltonian, and those in Fig. 5(a) and 2(a) are equivalent. The dash-dotted curves are the phase boundaries in the absence of Er^{3+} -magnon coupling (Er^{3+} - Fe^{3+} exchange interactions). The dashed curves are those obtained in the absence of Er^{3+} - Er^{3+} exchange interactions, i.e., the LTPT can be caused solely by the Er^{3+} -magnon coupling and thus can be interpreted as a magnonic SRPT.

hanced. These facts are similar to the suggestion of T_c enhancement through photon-matter coupling by G. Mazza and A. Georges [25], while their phase transition does not occur solely by the photon-matter coupling and their model does not guarantee gauge invariance [26, 27].

In order to quantitatively evaluate their contributions to the LTPT more in detail, we derive the condition for the SRPT in our extended Dicke Hamiltonian, Eq. (40), by using the Holstein-Primakoff transformation [55–57].

We rewrite $\hat{\Sigma}_{x,y,z}$ by the bosonic annihilation (creation) operator \hat{b} (\hat{b}^\dagger) as

$$\hat{\Sigma}_x \rightarrow \hat{b}^\dagger \hat{b} - \frac{N}{2}, \quad (53a)$$

$$\hat{\Sigma}_y \rightarrow \frac{\hat{b}^\dagger (N - \hat{b}^\dagger \hat{b})^{1/2} + (N - \hat{b}^\dagger \hat{b})^{1/2} \hat{b}}{2}, \quad (53b)$$

$$\hat{\Sigma}_z \rightarrow \frac{\hat{b}^\dagger (N - \hat{b}^\dagger \hat{b})^{1/2} - (N - \hat{b}^\dagger \hat{b})^{1/2} \hat{b}}{i2}. \quad (53c)$$

Further, we replace all the operators by c-numbers $\bar{a}_r, \bar{a}_i, \bar{b} \in \mathbb{R}$ as

$$\hat{a} \rightarrow \sqrt{N}(\bar{a}_r + i\bar{a}_i), \quad (54a)$$

$$\hat{b} \rightarrow i\sqrt{N}\bar{b}. \quad (54b)$$

Then, the Hamiltonian in Eq. (40) is transformed to

$$\frac{\hat{\mathcal{H}}}{N\hbar} \rightarrow \omega_\pi(\bar{a}_r^2 + \bar{a}_i^2) + \omega_{\text{Er}}\bar{b}^2 + \frac{4z_{\text{Er}}J_{\text{Er}}}{\hbar}\bar{b}^2(\bar{b}^2 - 1) + 2g_x\bar{a}_r(2\bar{b}^2 - 1) - 4g_z\bar{a}_i\bar{b}\sqrt{1 - \bar{b}^2} + \text{const.} \quad (55)$$

The ground state of the system should satisfy

$$\frac{1}{2} \frac{1}{\hbar N} \frac{\partial \mathcal{H}}{\partial \bar{a}_r} = \omega_\pi \bar{a}_r + g_x(2\bar{b}^2 - 1) = 0, \quad (56a)$$

$$\frac{1}{2} \frac{1}{\hbar N} \frac{\partial \mathcal{H}}{\partial \bar{a}_i} = \omega_\pi \bar{a}_i - 2g_z \bar{b} \sqrt{1 - \bar{b}^2} = 0, \quad (56b)$$

$$\frac{1}{2} \frac{1}{\hbar N} \frac{\partial \mathcal{H}}{\partial \bar{b}} = \omega_{\text{Er}} \bar{b} + \frac{4z_{\text{Er}}J_{\text{Er}}}{\hbar} \bar{b}(2\bar{b}^2 - 1) + 4g_x \bar{a}_r \bar{b} - 2g_z \bar{a}_i \frac{1 - 2\bar{b}^2}{\sqrt{1 - \bar{b}^2}} = 0. \quad (56c)$$

Solving the first two equations, we can express the Fe^{3+} qAFM magnon amplitudes as

$$\bar{a}_r = -\frac{g_x}{\omega_\pi}(2\bar{b}^2 - 1), \quad (57a)$$

$$\bar{a}_i = \frac{2g_z \bar{b} \sqrt{1 - \bar{b}^2}}{\omega_\pi}. \quad (57b)$$

Substituting these into Eq. (56c), we get an equation for the Er^{3+} amplitude as

$$\left[\omega_{\text{Er}} - \frac{4g_z^2 - 4g_x^2}{\omega_\pi} - \frac{4z_{\text{Er}}J_{\text{Er}}}{\hbar} \right. \\ \left. + \left(\frac{8g_z^2 - 8g_x^2}{\omega_\pi} + \frac{8z_{\text{Er}}J_{\text{Er}}}{\hbar} \right) \bar{b}^2 \right] \bar{b} = 0. \quad (58)$$

For a real nonzero value of \bar{b} to exist, the parameters must satisfy

$$\frac{4g_z^2}{\omega_\pi \omega_{\text{Er}}} - \frac{4g_x^2}{\omega_\pi \omega_{\text{Er}}} + \frac{4z_{\text{Er}}J_{\text{Er}}}{\hbar \omega_{\text{Er}}} > 1. \quad (59)$$

For $J_{\text{Er}} = g_x = 0$, this condition is reduced to $4g_z^2 > \omega_\pi \omega_{\text{Er}}$ for the SRPT in the Dicke model, Eq. (1).

The three terms on the left-hand side of Eq. (59) are evaluated as

$$D_{g_z} \equiv 4g_z^2 / (\omega_\pi \omega_{\text{Er}}) = 2.65, \quad (60a)$$

$$D_{g_x} \equiv -4g_x^2 / (\omega_\pi \omega_{\text{Er}}) = -0.51, \quad (60b)$$

$$D_{J_{\text{Er}}} \equiv 4z_{\text{Er}}J_{\text{Er}} / (\hbar \omega_{\text{Er}}) = 9.29. \quad (60c)$$

In the following, we call them *coupling depths*. They are dimensionless measures of coupling strengths and are definitely determined based on the appearance of the SRPT. As seen in Eq. (59), the SRPT occurs when the sum of these coupling depths is greater than unity: $D_{g_z} + D_{g_x} + D_{J_{\text{Er}}} > 1$. The coupling depth $D_{J_{\text{Er}}}$ of the J_{Er} term is the largest, which is consistent with Fig. 5. The g_x term (longitudinal coupling) gives a negative contribution for the SRPT ($D_{g_x} < 0$). Among the three couplings, the contribution of the g_z term is $D_{g_z} / (D_{g_z} + D_{g_x} + D_{J_{\text{Er}}}) = 0.23$,

and the contribution of the total Er^{3+} -magnon coupling is $(D_{g_z} + D_{g_x})/(D_{g_z} + D_{g_x} + D_{J_{\text{Er}}}) = 0.19$. These values are roughly equal to $1.3 \text{ K}/(1.3 \text{ K} + 3.4 \text{ K}) = 0.28$ estimated by Kadomtseva, Krynetskii, and Matveev [46], while they did not consider the longitudinal coupling (g_x term), which is not included in the cooperative Jahn-Teller model [47–50], and the parameters were determined only by the phase boundary for \mathbf{B}^{DC}/a .

From the viewpoint of the analogy between the two phase transitions, a remarkable fact is that the coupling depth of the g_z term satisfies $D_{g_z} > 1$ and $D_{g_z} + D_{g_x} > 1$. This suggests that the transverse Er^{3+} -magnon coupling is much stronger than the longitudinal one (giving the negative contribution) and ultrastrong enough to cause the SRPT solely. Also in this sense, we can conclude that the LTPT in ErFeO_3 is the magnonic SRPT obtained in the extended Dicke Hamiltonian with the direct atom-atom interaction and the longitudinal coupling (g_x term).

VIII. SUMMARY

From a spin model of ErFeO_3 that reproduces both the phase diagrams [34] and terahertz spectra [33], we derived an extended Dicke model that takes into account Er^{3+} - Er^{3+} exchange interactions as well as the cooperative coupling between Er^{3+} spins and Fe^{3+} magnon modes. We found that the LTPT in ErFeO_3 can be caused solely by the Er^{3+} -magnon coupling (in the absence of Er^{3+} - Er^{3+} exchange interactions), which demonstrates that the LTPT is a magnonic SRPT in the extended Dicke model.

In the thermodynamic limit, $N \rightarrow \infty$, the Dicke model is effectively interpreted as an infinite dimensional system [58], because the atoms interact equivalently with each other through the coupling with a single photonic mode. Such a dimensionality is reflected in critical exponents [58, 59] at phase transitions and would differentiate the LTPT in ErFeO_3 from standard magnetic phase transitions caused by short-range (nearest neighbor, next-nearest-neighbor, ...) exchange interactions between spins. Further, the coexistence of the direct (short-range) Er^{3+} - Er^{3+} interactions and Er^{3+} -magnon couplings (long-range retarded Er^{3+} - Er^{3+} interactions) in ErFeO_3 can lead to rich physics beyond what the normal Dicke model provides.

The thermal SRPT in ErFeO_3 would also give us rich physics compared with the quantum or zero-temperature SRPT that has been demonstrated by laser-driven cold atoms [7, 8]. In particular, it is known that the thermal and quantum fluctuations of photons and atoms show characteristic behaviors around the SRPT [59]. It is also known that the ground state of an ultrastrongly coupled system is a quantum squeezed vacuum even in the normal phase [3, 60–64], and strong two-mode squeezing at the SRPT has been demonstrated numerically [65]. Our on-going terahertz magnetospectroscopy experiments of $\text{Er}_x\text{Y}_{1-x}\text{FeO}_3$ around the LTPT [66] will experimentally examine such characteristic quantum squeezing at the thermal and quantum SRPTs.

ACKNOWLEDGMENTS

This research was supported by JST PRESTO program (grant JPMJPR1767), National Science Foundation (Cooperative Agreement DMR-1720595), and U.S. Army Research Office (grant W911NF-17-1-0259). We thank Andrey Baydin, Kenji Hayashida, Chien-Lung Huang, Takuma Makihara, Atsushi Miyake, Atsuhiko Miyata, and Fuyang Tay for fruitful discussion.

Appendix A: Mean-field Calculation

Since we simply consider an homogeneous external DC magnetic flux density \mathbf{B}^{DC} in this paper, the expectation values of Er^{3+} spins $\boldsymbol{\sigma}^{\text{A/B}} \equiv \langle \hat{\boldsymbol{\sigma}}_i^{\text{A/B}} \rangle$ and Fe^{3+} spins $\mathbf{S}^{\text{A/B}} \equiv \langle \hat{\mathbf{S}}_i^{\text{A/B}} \rangle$ are independent of the site index i . The bracket represents theoretically the expectation values of operators at finite temperature in the Heisenberg picture. It also corresponds to the ensemble average of the spins in each sublattice. Their equations of motion are obtained from the Heisenberg equations derived by the Hamiltonian in Eq. (7) as ($s = \text{A, B}$)

$$\hbar(\partial/\partial t)\boldsymbol{\sigma}^s = -\boldsymbol{\sigma}^s \times \mathbf{g}\mu_{\text{B}}\mathbf{B}_{\text{Er}}^s(\{\boldsymbol{\sigma}^{\text{A/B}}\}, \{\mathbf{S}^{\text{A/B}}\}), \quad (\text{A1a})$$

$$\hbar(\partial/\partial t)\mathbf{S}^s = -\mathbf{S}^s \times \mathbf{g}\mu_{\text{B}}\mathbf{B}_{\text{Fe}}^s(\{\boldsymbol{\sigma}^{\text{A/B}}\}, \{\mathbf{S}^{\text{A/B}}\}). \quad (\text{A1b})$$

Here, $\mathbf{B}_{\text{Er}}^{\text{A/B}}$ and $\mathbf{B}_{\text{Fe}}^{\text{A/B}}$ are the mean-fields for Er^{3+} and Fe^{3+} spins, respectively, and they are expressed as

$$\mathbf{g}\mu_{\text{B}}\mathbf{B}_{\text{Er}}^{\text{A}}(\{\boldsymbol{\sigma}^{\text{A/B}}\}, \{\mathbf{S}^{\text{A/B}}\}) = \mu_{\text{B}}\mathbf{g}^{\text{Er}} \cdot \mathbf{B}^{\text{DC}} + 2z_{\text{Er}}J_{\text{Er}}\boldsymbol{\sigma}^{\text{B}} + \sum_{s=\text{A,B}} 2 \begin{pmatrix} JS_x^s - (\mathbf{D}^{\text{A},s} \times \mathbf{S}^s)_x \\ 0 \\ JS_z^s - (\mathbf{D}^{\text{A},s} \times \mathbf{S}^s)_z \end{pmatrix}, \quad (\text{A2a})$$

$$\mathbf{g}\mu_{\text{B}}\mathbf{B}_{\text{Er}}^{\text{B}}(\{\boldsymbol{\sigma}^{\text{A/B}}\}, \{\mathbf{S}^{\text{A/B}}\}) = \mu_{\text{B}}\mathbf{g}^{\text{Er}} \cdot \mathbf{B}^{\text{DC}} + 2z_{\text{Er}}J_{\text{Er}}\boldsymbol{\sigma}^{\text{A}} + \sum_{s=\text{A,B}} 2 \begin{pmatrix} JS_x^s - (\mathbf{D}^{\text{B},s} \times \mathbf{S}^s)_x \\ 0 \\ JS_z^s - (\mathbf{D}^{\text{B},s} \times \mathbf{S}^s)_z \end{pmatrix}, \quad (\text{A2b})$$

$$\begin{aligned} \mathfrak{g}\mu_B \mathbf{B}_{\text{Fe}}^A(\{\boldsymbol{\sigma}^{A/B}\}, \{\mathbf{S}^{A/B}\}) &= \mu_B \mathfrak{g}^{\text{Fe}} \cdot \mathbf{B}^{\text{DC}} + \sum_{s=A,B} x (J\boldsymbol{\sigma}^s + \mathbf{D}^{s,A} \times \boldsymbol{\sigma}^s) \\ &+ \left(\begin{array}{c} z_{\text{Fe}} J_{\text{Fe}} S_x^B + z_{\text{Fe}} D_y^{\text{Fe}} S_z^B - 2A_x S_x^A - A_{xz} S_z^A \\ z_{\text{Fe}} J_{\text{Fe}} S_z^B - z_{\text{Fe}} D_y^{\text{Fe}} S_x^B - 2A_z S_z^A - A_{xz} S_x^A \end{array} \right), \end{aligned} \quad (\text{A2c})$$

$$\begin{aligned} \mathfrak{g}\mu_B \mathbf{B}_{\text{Fe}}^B(\{\boldsymbol{\sigma}^{A/B}\}, \{\mathbf{S}^{A/B}\}) &= \mu_B \mathfrak{g}^{\text{Fe}} \cdot \mathbf{B}^{\text{DC}} + \sum_{s=A,B} x (J\boldsymbol{\sigma}^s + \mathbf{D}^{s,B} \times \boldsymbol{\sigma}^s) \\ &+ \left(\begin{array}{c} z_{\text{Fe}} J_{\text{Fe}} S_x^A - z_{\text{Fe}} D_y^{\text{Fe}} S_z^A - 2A_x S_x^B + A_{xz} S_z^B \\ z_{\text{Fe}} J_{\text{Fe}} S_z^A + z_{\text{Fe}} D_y^{\text{Fe}} S_x^A - 2A_z S_z^B + A_{xz} S_x^B \end{array} \right). \end{aligned} \quad (\text{A2d})$$

In Eqs. (A2a) and (A2b), the first, second, and third terms represent the Zeeman effect, Er^{3+} - Er^{3+} exchange interaction, and Er^{3+} - Fe^{3+} exchange interaction, respectively. In Eqs. (A2c) and (A2d), the first, second, and third terms represent the Zeeman effect, Er^{3+} - Fe^{3+} exchange interaction, and Fe^{3+} - Fe^{3+} exchange interaction, respectively. The dilution of Er^{3+} spins is reflected through the factors $z_{\text{Er}} = 6x$ and x , i.e., the number of neighboring Er^{3+} is effectively decreased by factor x . Since $(1/2)\hat{\boldsymbol{\sigma}}^{A/B}$ corresponds to the spin- $\frac{1}{2}$ operator, the factor 2 appears overall in Eqs. (A2a) and (A2b). As explained at the end of Sec. IV, the y component of the third term in Eqs. (A2a) and (A2b) is set to be zero by implicitly considering a high energy potential.

The free energy of the system is minimized when the thermal-equilibrium values (time-averages) of spins $\bar{\boldsymbol{\sigma}}^{A/B}$ and $\bar{\mathbf{S}}^{A/B}$ are parallel to their mean-fields $\bar{\mathbf{B}}_{\text{Er}}^s \equiv \mathbf{B}_{\text{Er}}^s(\{\bar{\boldsymbol{\sigma}}^{A/B}\}, \{\bar{\mathbf{S}}^{A/B}\})$ and $\bar{\mathbf{B}}_{\text{Fe}}^s \equiv \mathbf{B}_{\text{Fe}}^s(\{\bar{\boldsymbol{\sigma}}^{A/B}\}, \{\bar{\mathbf{S}}^{A/B}\})$ as

$$\bar{\boldsymbol{\sigma}}^s = \langle \hat{\boldsymbol{\sigma}}^s \rangle = \langle \hat{\sigma}_{\parallel}^s \rangle \mathbf{u}_{\text{Er}}^s, \quad \hat{\sigma}_{\parallel}^s \equiv \hat{\boldsymbol{\sigma}}^s \cdot \mathbf{u}_{\text{Er}}^s, \quad (\text{A3a})$$

$$\bar{\mathbf{S}}^s = \langle \hat{\mathbf{S}}^s \rangle = \langle \hat{S}_{\parallel}^s \rangle \mathbf{u}_{\text{Fe}}^s, \quad \hat{S}_{\parallel}^s \equiv \hat{\mathbf{S}}^s \cdot \mathbf{u}_{\text{Fe}}^s, \quad (\text{A3b})$$

where we defined unit vectors of the mean-fields as

$$\mathbf{u}_{\text{Er}}^s \equiv \bar{\mathbf{B}}_{\text{Er}}^s / |\bar{\mathbf{B}}_{\text{Er}}^s|, \quad (\text{A4a})$$

$$\mathbf{u}_{\text{Fe}}^s \equiv \bar{\mathbf{B}}_{\text{Fe}}^s / |\bar{\mathbf{B}}_{\text{Fe}}^s|. \quad (\text{A4b})$$

The thermal-equilibrium values $\bar{\boldsymbol{\sigma}}^{A/B}$ and $\bar{\mathbf{S}}^{A/B}$ are determined as follows. For given mean-fields $\bar{\mathbf{B}}_{\text{Fe}}^s$ and $\bar{\mathbf{B}}_{\text{Er}}^s$, effective Hamiltonians of each Er^{3+} and Fe^{3+} can be defined, respectively, as

$$\hat{\mathcal{H}}_{\text{Er}}^s = \frac{1}{2} \mathfrak{g}\mu_B \hat{\boldsymbol{\sigma}}^s \cdot \bar{\mathbf{B}}_{\text{Er}}^s = \frac{1}{2} \mathfrak{g}\mu_B \hat{\sigma}_{\parallel}^s |\bar{\mathbf{B}}_{\text{Er}}^s|, \quad (\text{A5a})$$

$$\hat{\mathcal{H}}_{\text{Fe}}^s = \mathfrak{g}\mu_B \hat{\mathbf{S}}^s \cdot \bar{\mathbf{B}}_{\text{Fe}}^s = \mathfrak{g}\mu_B \hat{S}_{\parallel}^s |\bar{\mathbf{B}}_{\text{Fe}}^s|. \quad (\text{A5b})$$

Then, the partition functions are expressed as

$$\begin{aligned} Z_{\text{Er}}^s &\equiv \text{Tr} \left[e^{-\hat{\mathcal{H}}_{\text{Er}}^s / (k_B T)} \right] = \sum_{m=\pm 1} e^{-m y_s} \\ &= 2 \cosh(y_s), \end{aligned} \quad (\text{A6a})$$

$$\begin{aligned} Z_{\text{Fe}}^s &\equiv \text{Tr} \left[e^{-\hat{\mathcal{H}}_{\text{Fe}}^s / (k_B T)} \right] = \sum_{m=-S}^S e^{-m x_s} \\ &= \frac{\sinh[(S + 1/2)x_j]}{\sinh(x_s/2)}, \end{aligned} \quad (\text{A6b})$$

where we defined

$$y_s \equiv \mathfrak{g}\mu_B |\bar{\mathbf{B}}_{\text{Er}}^s| / (2k_B T), \quad (\text{A7a})$$

$$x_s \equiv \mathfrak{g}\mu_B |\bar{\mathbf{B}}_{\text{Fe}}^s| / (k_B T). \quad (\text{A7b})$$

Since $\hat{\boldsymbol{\sigma}}^{A/B}$ is not a standard spin operator with an angular momentum of \hbar or $\hbar/2$ but is a vector of the Pauli operators, the summation is performed for $m = \pm 1$. The free energies are given as $-k_B T \ln Z_{\text{Er}}^{A/B}$ and $-k_B T \ln Z_{\text{Fe}}^{A/B}$, and the thermal-equilibrium values of the spins are obtained as

$$\langle \hat{\sigma}_{\parallel}^s \rangle = -\frac{\partial}{\partial y_s} \ln Z_{\text{Er}}^s = -\tanh(y_s), \quad (\text{A8a})$$

$$\langle \hat{S}_{\parallel}^s \rangle = -\frac{\partial}{\partial x_s} \ln Z_{\text{Fe}}^s = -S B_S(S x_s), \quad (\text{A8b})$$

where $B_S(z)$ is the Brillouin function defined as

$$B_J(z) \equiv \frac{2J+1}{2J} \coth\left(\frac{2J+1}{2J}z\right) - \frac{1}{2J} \coth\left(\frac{z}{2J}\right). \quad (\text{A9})$$

By consistently solving Eqs. (A2), (A3), and (A8), we can determine $\bar{\boldsymbol{\sigma}}^{A/B}$ and $\bar{\mathbf{S}}^{A/B}$ at finite temperatures.

Appendix B: Reduction of number of parameters

In this appendix, we reduce the number of parameters in our spin model by considering the spin configuration in the Γ_{12} phase of ErFeO_3 when the external DC magnetic field is zero or along the a axis. In the ground

state ($T = 0$), the equilibrium values of the spins satisfies Eqs. (A1) with $(\partial/\partial t)\mathbf{R}^{A/B} = 0$ and $(\partial/\partial t)\mathbf{S}^{A/B} = 0$. Here, as depicted in Fig. 1, due to the π -rotational symmetry about the a axis, we represent the four spins $\mathbf{R}^{A/B}$ and $\mathbf{S}^{A/B}$ (twelve elements) by six values as

$$R_x^A = R_x^B \equiv \mathcal{R}_x, \quad (\text{B1a})$$

$$R_y^A = -R_y^B \equiv \mathcal{R}_y, \quad (\text{B1b})$$

$$R_z^A = -R_z^B \equiv \mathcal{R}_z, \quad (\text{B1c})$$

$$S_x^A = S_x^B \equiv \mathcal{S}_x, \quad (\text{B1d})$$

$$S_y^A = -S_y^B \equiv \mathcal{S}_y, \quad (\text{B1e})$$

$$-S_z^A = S_z^B \equiv \mathcal{S}_z. \quad (\text{B1f})$$

Using these and Eqs. (A1) and (A2), we get

$$\begin{pmatrix} \mathcal{R}_x \\ \mathcal{R}_y \\ \mathcal{R}_z \end{pmatrix} \times \left[\begin{pmatrix} \mathbf{g}_x^{\text{Er}} \mu_B B^{\text{DC}} \\ 0 \\ 0 \end{pmatrix} + 2z_{\text{Er}} J_{\text{Er}} \begin{pmatrix} \mathcal{R}_x \\ -\mathcal{R}_y \\ -\mathcal{R}_z \end{pmatrix} + 4 \begin{pmatrix} J_{A,+} \mathcal{S}_x + D_{A,-,y} \mathcal{S}_z + D_{A,-,z} \mathcal{S}_y \\ J_{A,-} \mathcal{S}_y - D_{A,+,z} \mathcal{S}_x - D_{A,-,x} \mathcal{S}_z \\ -J_{A,-} \mathcal{S}_z - D_{A,-,x} \mathcal{S}_y + D_{A,+,y} \mathcal{S}_x \end{pmatrix} \right] = \mathbf{0}, \quad (\text{B2a})$$

$$\begin{pmatrix} \mathcal{R}_x \\ -\mathcal{R}_y \\ -\mathcal{R}_z \end{pmatrix} \times \left[\begin{pmatrix} \mathbf{g}_x^{\text{Er}} \mu_B B^{\text{DC}} \\ 0 \\ 0 \end{pmatrix} + 2z_{\text{Er}} J_{\text{Er}} \begin{pmatrix} \mathcal{R}_x \\ \mathcal{R}_y \\ \mathcal{R}_z \end{pmatrix} + 4 \begin{pmatrix} J_{B,+} \mathcal{S}_x + D_{B,-,y} \mathcal{S}_z + D_{B,-,z} \mathcal{S}_y \\ J_{B,-} \mathcal{S}_y - D_{B,+,z} \mathcal{S}_x - D_{B,-,x} \mathcal{S}_z \\ -J_{B,-} \mathcal{S}_z - D_{B,-,x} \mathcal{S}_y + D_{B,+,y} \mathcal{S}_x \end{pmatrix} \right] = \mathbf{0}, \quad (\text{B2b})$$

$$\begin{pmatrix} \mathcal{S}_x \\ \mathcal{S}_y \\ -\mathcal{S}_z \end{pmatrix} \times \left\{ \begin{pmatrix} \mathbf{g}_x^{\text{Fe}} \mu_B B^{\text{DC}} \\ 0 \\ 0 \end{pmatrix} + 2x \begin{pmatrix} J_{+,A} \mathcal{R}_x + D_{-,A,y} \mathcal{R}_z - D_{-,A,z} \mathcal{R}_y \\ J_{-,A} \mathcal{R}_y + D_{+,A,z} \mathcal{R}_x - D_{-,A,x} \mathcal{R}_z \\ J_{-,A} \mathcal{R}_z + D_{-,A,x} \mathcal{R}_y - D_{+,A,y} \mathcal{R}_x \end{pmatrix} \right. \\ \left. + \begin{pmatrix} (z_{\text{Fe}} J_{\text{Fe}} - 2A_x) \mathcal{S}_x + (z_{\text{Fe}} D_z^{\text{Fe}} - A_{xy}) \mathcal{S}_y + (z_{\text{Fe}} D_y^{\text{Fe}} + A_{xz}) \mathcal{S}_z \\ (z_{\text{Fe}} D_z^{\text{Fe}} - A_{xy}) \mathcal{S}_x - (z_{\text{Fe}} J_{\text{Fe}} + 2A_y) \mathcal{S}_y \\ -(z_{\text{Fe}} D_y^{\text{Fe}} + A_{xz}) \mathcal{S}_x + (z_{\text{Fe}} J_{\text{Fe}} + 2A_z) \mathcal{S}_z \end{pmatrix} \right\} = \mathbf{0}, \quad (\text{B2c})$$

$$\begin{pmatrix} \mathcal{S}_x \\ -\mathcal{S}_y \\ \mathcal{S}_z \end{pmatrix} \times \left\{ \begin{pmatrix} \mathbf{g}_x^{\text{Fe}} \mu_B B^{\text{DC}} \\ 0 \\ 0 \end{pmatrix} + 2x \begin{pmatrix} J_{+,B} \mathcal{R}_x + D_{-,B,y} \mathcal{R}_z - D_{-,B,z} \mathcal{R}_y \\ J_{-,B} \mathcal{R}_y + D_{+,B,z} \mathcal{R}_x - D_{-,B,x} \mathcal{R}_z \\ J_{-,B} \mathcal{R}_z + D_{-,B,x} \mathcal{R}_y - D_{+,B,y} \mathcal{R}_x \end{pmatrix} \right. \\ \left. + \begin{pmatrix} (z_{\text{Fe}} J_{\text{Fe}} - 2A_x) \mathcal{S}_x + (z_{\text{Fe}} D_z^{\text{Fe}} - A_{xy}) \mathcal{S}_y + (z_{\text{Fe}} D_y^{\text{Fe}} + A_{xz}) \mathcal{S}_z \\ -(z_{\text{Fe}} D_z^{\text{Fe}} - A_{xy}) \mathcal{S}_x + (z_{\text{Fe}} J_{\text{Fe}} + 2A_y) \mathcal{S}_y \\ (z_{\text{Fe}} D_y^{\text{Fe}} + A_{xz}) \mathcal{S}_x - (z_{\text{Fe}} J_{\text{Fe}} + 2A_z) \mathcal{S}_z \end{pmatrix} \right\} = \mathbf{0}, \quad (\text{B2d})$$

where we defined

$$J_{s,\pm} \equiv (J_{s,A} \pm J_{s,B})/2, \quad (\text{B3a})$$

$$J_{\pm,s} \equiv (J_{A,s} \pm J_{B,s})/2, \quad (\text{B3b})$$

$$\mathbf{D}^{s,\pm} \equiv (\mathbf{D}^{s,A} \pm \mathbf{D}^{s,B})/2, \quad (\text{B3c})$$

$$\mathbf{D}^{\pm,s} \equiv (\mathbf{D}^{A,s} \pm \mathbf{D}^{B,s})/2. \quad (\text{B3d})$$

For the equivalence between Eq. (B2c) and Eq. (B2d), the following equations should be satisfied for any $\mathcal{R}_{x,y,z}$:

$$J_{+,A} \mathcal{R}_x + D_{-,A,y} \mathcal{R}_z - D_{-,A,z} \mathcal{R}_y = J_{+,B} \mathcal{R}_x + D_{-,B,y} \mathcal{R}_z - D_{-,B,z} \mathcal{R}_y, \quad (\text{B4a})$$

$$J_{-,A} \mathcal{R}_y + D_{+,A,z} \mathcal{R}_x - D_{-,A,x} \mathcal{R}_z = -J_{-,B} \mathcal{R}_y - D_{+,B,z} \mathcal{R}_x + D_{-,B,x} \mathcal{R}_z, \quad (\text{B4b})$$

$$J_{-,A} \mathcal{R}_z + D_{-,A,x} \mathcal{R}_y - D_{+,A,y} \mathcal{R}_x = -J_{-,B} \mathcal{R}_z - D_{-,B,x} \mathcal{R}_y + D_{+,B,y} \mathcal{R}_x. \quad (\text{B4c})$$

Then, we get the following relations:

$$J_{+,A} = J_{+,B}, \quad (\text{B5a})$$

$$J_{-,A} = -J_{-,B}, \quad (\text{B5b})$$

$$D_{-,A,x} = -D_{-,B,x}, \quad (\text{B5c})$$

$$D_{+,A,y} = -D_{+,B,y}, \quad (\text{B5d})$$

$$D_{-,A,y} = D_{-,B,y}, \quad (\text{B5e})$$

$$D_{+,A,z} = -D_{+,B,z}, \quad (\text{B5f})$$

$$D_{-,A,z} = D_{-,B,z}. \quad (\text{B5g})$$

On the other hand, for the equivalence between Eq. (B2a) and Eq. (B2b) incorporating the consistency with Eqs. (B5), the following equations should be satisfied for any $\mathcal{S}_{x,y,z}$:

$$J_{A,+}\mathcal{S}_x + D_{A,-,y}\mathcal{S}_z + D_{A,-,z}\mathcal{S}_y = J_{B,+}\mathcal{S}_x + D_{B,-,y}\mathcal{S}_z + D_{B,-,z}\mathcal{S}_y, \quad (\text{B6a})$$

$$J_{A,-}\mathcal{S}_y - D_{A,+,z}\mathcal{S}_x - D_{A,-,x}\mathcal{S}_z = -(J_{B,-}\mathcal{S}_y - D_{B,+,z}\mathcal{S}_x - D_{B,-,x}\mathcal{S}_z), \quad (\text{B6b})$$

$$-J_{A,-}\mathcal{S}_z - D_{A,-,x}\mathcal{S}_y + D_{A,+,y}\mathcal{S}_x = -(-J_{B,-}\mathcal{S}_z - D_{B,-,x}\mathcal{S}_y + D_{B,+,y}\mathcal{S}_x). \quad (\text{B6c})$$

Then, we get the following relations:

$$J_{A,+} = J_{B,+}, \quad (\text{B7a})$$

$$J_{A,-} = -J_{B,-}, \quad (\text{B7b})$$

$$D_{A,-,x} = -D_{B,-,x}, \quad (\text{B7c})$$

$$D_{A,+,y} = -D_{B,+,y}, \quad (\text{B7d})$$

$$D_{A,-,y} = D_{B,-,y}, \quad (\text{B7e})$$

$$D_{A,+,z} = -D_{B,+,z}, \quad (\text{B7f})$$

$$D_{A,-,z} = D_{B,-,z}. \quad (\text{B7g})$$

A possible choice of parameters for satisfying Eqs. (B5) and (B7) is

$$J_{A,A} = J_{B,B} = J + J', \quad J_{A,B} = J_{B,A} = J - J', \quad (\text{B8a})$$

$$\mathbf{D}^{A,A} = \begin{pmatrix} D_x + D'_x \\ D_y + D'_y \\ D_z + D'_z \end{pmatrix}, \quad \mathbf{D}^{A,B} = \begin{pmatrix} -D_x + D'_x \\ -D_y + D'_y \\ -D_z + D'_z \end{pmatrix},$$

$$\mathbf{D}^{B,A} = \begin{pmatrix} -D_x + D'_x \\ D_y - D'_y \\ D_z - D'_z \end{pmatrix}, \quad \mathbf{D}^{B,B} = \begin{pmatrix} D_x + D'_x \\ -D_y - D'_y \\ -D_z - D'_z \end{pmatrix}. \quad (\text{B8b})$$

Among these eight parameters J , J' , $D_{x,y,z}$, and $D'_{x,y,z}$, we numerically found by the mean-field calculation that $J' = D'_y = D'_z = 0$ must be satisfied in order to make the LTPT a second-order phase transition. Otherwise, it becomes a crossover between the Γ_{12} and Γ_2 phases. Further, D'_x and D'_z gives negligible effects on the phase diagrams under the present parameters. Therefore, we consider only J , D_x , and D_y in the spin model discussed in the main text.

Appendix C: Spin resonance frequencies

In this Appendix, we discuss spin resonance frequencies (especially frequency anti-crossing) at $T > T_c$ (Γ_2 phase) in the presence of the external DC magnetic field along the a , b , and c axes. By fitting the calculated resonance frequencies to the peak positions in THz spectra obtained in our previous experimental study [33], we determine some parameters (J_{Er} , J , D_y , and A_x) in our spin model as we explain in Appendix D. We show also the consistency between the results by the two approaches: the mean-field calculation and the extended Dicke Hamiltonian.

In the mean-field approach, the spin resonance frequencies will be calculated based on Eqs. (A1), from which equations of motion of the spin fluctuations $\delta\boldsymbol{\sigma}^{A/B}(t) \equiv \boldsymbol{\sigma}^{A/B}(t) - \bar{\boldsymbol{\sigma}}^{A/B}$ and $\delta\mathbf{S}^{A/B}(t) \equiv \mathbf{S}^{A/B}(t) - \bar{\mathbf{S}}^{A/B}$ are obtained as ($s = A, B$)

$$\begin{aligned} \hbar(\partial/\partial t)\delta\boldsymbol{\sigma}^s &= -\delta\boldsymbol{\sigma}^s \times \mathbf{g}\mu_B\bar{\mathbf{B}}_{\text{Er}}^s \\ &\quad - \bar{\boldsymbol{\sigma}}^s \times \mathbf{g}\mu_B\mathbf{B}_{\text{Er}}^s(\{\delta\boldsymbol{\sigma}^{A/B}\}, \{\delta\mathbf{S}^{A/B}\}), \end{aligned} \quad (\text{C1a})$$

$$\begin{aligned} \hbar(\partial/\partial t)\delta\mathbf{S}^s &= -\delta\mathbf{S}^s \times \mathbf{g}\mu_B\bar{\mathbf{B}}_{\text{Fe}}^s \\ &\quad - \bar{\mathbf{S}}^s \times \mathbf{g}\mu_B\mathbf{B}_{\text{Fe}}^s(\{\delta\boldsymbol{\sigma}^{A/B}\}, \{\delta\mathbf{S}^{A/B}\}). \end{aligned} \quad (\text{C1b})$$

From eigenvalues E_k of the 12×12 coefficient matrix for $\delta\boldsymbol{\sigma}^{A/B}$ and $\delta\mathbf{S}^{A/B}$ on the right-hand sides, we can find four positive eigenfrequencies of the spin resonances as $\nu_k = iE_k/h$. Another four are negative, and the other four are zero. The temperature used for determining the equilibrium spins $\bar{\boldsymbol{\sigma}}^{A/B}$ and $\bar{\mathbf{S}}^{A/B}$ will be assumed as $T = 20 \text{ K} > T_c$. While it is higher than the cryostat temperature 10 K used for measuring the THz spectrum (shown in Fig. 8), $T = 20 \text{ K}$ is better suited for reproducing the experimental spectrum. The reason remains as a future problem.

We will also calculate the spin resonance frequencies from the extended Dicke Hamiltonian, Eq. (37). We will see that the five Er^{3+} -magnon couplings show a variety of frequency anti-crossings. It originates from the fact that the Fe^{3+} qFM ($K = 0$) and qAFM ($K = \pi$) magnon modes and the Er^{3+} spin resonances in the A and B sublattices are all coupled in general as seen in the extended Dicke Hamiltonian.

Note that the actual Hamiltonian treated in this Appendix is

$$\begin{aligned} \hat{\mathcal{H}} &\approx \sum_{K=0,\pi} \hbar\omega_K \hat{a}_K^\dagger \hat{a}_K + E_x \hat{\Sigma}_x^+ + \sum_{\xi=x,y,z} \mathbf{g}_\xi^{\text{Er}} \mu_B B_\xi^{\text{DC}} \hat{\Sigma}_\xi^+ \\ &\quad + \frac{8z_{\text{Er}} J_{\text{Er}}}{N} \hat{\Sigma}^A \cdot \hat{\Sigma}^B + \frac{2\hbar g_x}{\sqrt{N}} (\hat{a}_\pi^\dagger + \hat{a}_\pi) \delta\hat{\Sigma}_x^+ \\ &\quad + \frac{i2\hbar g_y}{\sqrt{N}} (\hat{a}_0^\dagger - \hat{a}_0) \delta\hat{\Sigma}_y^+ + \frac{2\hbar g'_y}{\sqrt{N}} (\hat{a}_\pi^\dagger + \hat{a}_\pi) \delta\hat{\Sigma}_y^- \\ &\quad + \frac{i2\hbar g_z}{\sqrt{N}} (\hat{a}_\pi^\dagger - \hat{a}_\pi) \delta\hat{\Sigma}_z^- + \frac{2\hbar g'_z}{\sqrt{N}} (\hat{a}_0^\dagger + \hat{a}_0) \delta\hat{\Sigma}_z^+. \end{aligned} \quad (\text{C2})$$

Compared with Eq. (37), the Er^{3+} spin operators $\hat{\Sigma}_{x,y,z}^\pm$ in the coupling terms are replaced by their fluctuations $\delta\hat{\Sigma}_{x,y,z}^\pm \equiv \hat{\Sigma}_{x,y,z}^\pm - \bar{\Sigma}_{x,y,z}^\pm$. The terms including the equi-

librium values $\bar{\Sigma}_{x,y,z}^\pm$ give shifts of Fe^{3+} magnon frequencies. However, returning to Eq. (32), we can find that the influence of these terms is smaller by factor $N_0^{-1/2}$ than the magnon Hamiltonian $\sum_{K=0,\pi} \hbar\omega_K \hat{a}_K^\dagger \hat{a}_K$. Then, the equilibrium values $\bar{\Sigma}_{x,y,z}^\pm$ can be omitted in Eq. (C2).

We will calculate the eigenfrequencies of Eq. (C2). However, since we suppose the Γ_2 phase ($T > T_c$) in this Appendix, we do not consider the spontaneous ordering of Er^{3+} spins nor the rotation of the Fe^{3+} spins in the calculation of the eigenfrequencies. Then, the results are justified only for relatively high external DC field that makes the system in the Γ_2 phase even in the zero-temperature limit.

In the calculation based on the extended Dicke Hamiltonian, the finite temperature ($T = 20$ K) is incorporated in the following procedure. We consider the thermal excitation of the Er^{3+} spins and assume that the Er^{3+} density effectively depends on the temperature as [33]

$$x = \tanh\left(\frac{E_{\text{Er}}}{2k_{\text{B}}T}\right), \quad (\text{C3})$$

where the Er^{3+} excitation energy E_{Er} (excluding the Er^{3+} - Er^{3+} exchange interaction) is represented as

$$E_{\text{Er}} \equiv \sqrt{(E_x + \mathfrak{g}_x^{\text{Er}} \mu_{\text{B}} B_x^{\text{DC}})^2 + \sum_{\xi=y,z} (\mathfrak{g}_\xi^{\text{Er}} \mu_{\text{B}} B_\xi^{\text{DC}})^2}. \quad (\text{C4})$$

The temperature dependence appears through this effective x and $z_{\text{Er}} = 6x$.

Note that, in this Appendix, the results by the mean-field approach is more reliable than those by the extended Dicke Hamiltonian, which are derived under some approximations. However, the spin resonance frequencies and anti-crossing on them will be better clarified by the extended Dicke Hamiltonian.

In the following subsections, we discuss how the five Er^{3+} -magnon couplings are reflected in three configurations: $\mathbf{B}^{\text{DC}}//a$ (Appendix C 1), $\mathbf{B}^{\text{DC}}//b$ (Appendix C 2), and $\mathbf{B}^{\text{DC}}//c$ (Appendix C 3). We compare them with our experimental results [33] in Appendix C 4.

1. $\mathbf{B}^{\text{DC}}//a$

If the external DC magnetic field is along the a axis, the Er^{3+} subsystem is most stable when the Er^{3+} spins are along the a axis. For calculating the spin resonance frequencies from the extended Dicke Hamiltonian in the weak excitation limit (linear optical response), we here bosonize the spin operators. By the lowest-order Holstein-Primakoff transformation, the spin- $\frac{N}{4}$ operators are transformed as ($s = \text{A,B}$)

$$\hat{\Sigma}_x^s \rightarrow \hat{b}_s^\dagger \hat{b}_s - \frac{N}{4}, \quad (\text{C5a})$$

$$\delta \hat{\Sigma}_x^s \rightarrow \hat{b}_s^\dagger \hat{b}_s \quad (\text{C5b})$$

$$\hat{\Sigma}_y^s = \delta \hat{\Sigma}_y^s \rightarrow \sqrt{\frac{N}{2}} \frac{\hat{b}_s^\dagger + \hat{b}_s}{2}, \quad (\text{C5c})$$

$$\hat{\Sigma}_z^s = \delta \hat{\Sigma}_z^s \rightarrow \sqrt{\frac{N}{2}} \frac{\hat{b}_s^\dagger - \hat{b}_s}{i2}. \quad (\text{C5d})$$

Then, the total Hamiltonian in Eq. (C2) is transformed as

$$\begin{aligned} \hat{\mathcal{H}} \approx & \sum_{K=0,\pi} \hbar\omega_K \hat{a}_K^\dagger \hat{a}_K + (E_x + \mathfrak{g}_x^{\text{Er}} \mu_{\text{B}} B_x^{\text{DC}}) (\hat{b}_+^\dagger \hat{b}_+ + \hat{b}_-^\dagger \hat{b}_-) \\ & - 4z_{\text{Er}} J_{\text{Er}} \hat{b}_-^\dagger \hat{b}_- + \hbar g_x (\hat{a}_\pi^\dagger + \hat{a}_\pi) (\hat{b}_+^\dagger \hat{b}_+ + \hat{b}_-^\dagger \hat{b}_-) \\ & + i\hbar g_y (\hat{a}_0^\dagger - \hat{a}_0) (\hat{b}_+^\dagger + \hat{b}_+) + \hbar g_y' (\hat{a}_\pi^\dagger + \hat{a}_\pi) (\hat{b}_-^\dagger + \hat{b}_-) \\ & + \hbar g_z (\hat{a}_\pi^\dagger - \hat{a}_\pi) (\hat{b}_-^\dagger - \hat{b}_-) - i\hbar g_z' (\hat{a}_0^\dagger + \hat{a}_0) (\hat{b}_+^\dagger - \hat{b}_+) \\ & + \text{const.} \end{aligned} \quad (\text{C6})$$

Here, we defined operators of the in-phase oscillation \hat{b}_+ and out-of-phase one \hat{b}_- of the two Er^{3+} spins $\hat{b}_{\text{A/B}}$ as

$$\hat{b}_\pm = \frac{\hat{b}_{\text{A}} \pm \hat{b}_{\text{B}}}{\sqrt{2}}. \quad (\text{C7})$$

In the weak excitation limit, the g_x term can be neglected, since it is involved with the number of Er^{3+} excitations $\hat{b}_\pm^\dagger \hat{b}_\pm$. Then, the Hamiltonian can be divided into two parts as

$$\hat{\mathcal{H}} \approx \hat{\mathcal{H}}_{0+} + \hat{\mathcal{H}}_{\pi-} + \text{const.} \quad (\text{C8})$$

The first term consists of the Fe^{3+} qFM magnon mode and Er^{3+} in-phase mode, and it is expressed as

$$\begin{aligned} \hat{\mathcal{H}}_{0+} \equiv & \hbar\omega_0 \hat{a}_0^\dagger \hat{a}_0 + |E_x + \mathfrak{g}_x^{\text{Er}} \mu_{\text{B}} B_x^{\text{DC}}| \hat{b}_+^\dagger \hat{b}_+ + i\hbar g_y (\hat{a}_0^\dagger - \hat{a}_0) (\hat{b}_+^\dagger + \hat{b}_+) \\ & - i\hbar g_z' (\hat{a}_0^\dagger + \hat{a}_0) \times \begin{cases} (\hat{b}_+^\dagger - \hat{b}_+) & \mathfrak{g}_x^{\text{Er}} \mu_{\text{B}} B_x^{\text{DC}} > -E_x \\ (\hat{b}_+ - \hat{b}_+^\dagger) & \mathfrak{g}_x^{\text{Er}} \mu_{\text{B}} B_x^{\text{DC}} < -E_x \end{cases} \end{aligned} \quad (\text{C9})$$

If the coefficient ($E_x + \mathfrak{g}_x^{\text{Er}} \mu_{\text{B}} B_x^{\text{DC}}$) of the second term in Eq. (C6) is negative for negative B_x^{DC} , the roles of the annihilation operator \hat{b}_+ and creation one \hat{b}_+^\dagger are flipped. As a result of it, the sign of the last term in Eq. (C9) was flipped. On the other hand, the second term in Eq. (C8) consists of the Fe^{3+} qAFM magnon mode and Er^{3+}

out-of-phase mode, and it is expressed as

$$\begin{aligned} \hat{\mathcal{H}}_{\pi-} &\equiv \hbar\omega_{\pi}\hat{a}_{\pi}^{\dagger}\hat{a}_{\pi} + \hbar g'_y(\hat{a}_{\pi}^{\dagger} + \hat{a}_{\pi})(\hat{b}_{-}^{\dagger} + \hat{b}_{-}) \\ &+ \begin{cases} (E_x + \mathfrak{g}_x^{\text{Er}}\mu_B B_x^{\text{DC}} - 4z_{\text{Er}}J_{\text{Er}})\hat{b}_{-}^{\dagger}\hat{b}_{-} + \hbar g_z(\hat{a}_{\pi}^{\dagger} - \hat{a}_{\pi})(\hat{b}_{-}^{\dagger} - \hat{b}_{-}) & \mathfrak{g}_x^{\text{Er}}\mu_B B_x^{\text{DC}} > -E_x + 4z_{\text{Er}}J_{\text{Er}} \\ (-E_x - \mathfrak{g}_x^{\text{Er}}\mu_B B_x^{\text{DC}} - 4z_{\text{Er}}J_{\text{Er}})\hat{b}_{-}^{\dagger}\hat{b}_{-} + \hbar g_z(\hat{a}_{\pi}^{\dagger} - \hat{a}_{\pi})(\hat{b}_{-} - \hat{b}_{-}^{\dagger}) & \mathfrak{g}_x^{\text{Er}}\mu_B B_x^{\text{DC}} < -E_x - 4z_{\text{Er}}J_{\text{Er}} \end{cases} \quad (\text{C10}) \end{aligned}$$

The $\text{Er}^{3+}\text{-Er}^{3+}$ exchange interaction, the third term in Eq. (C6), gives a negative frequency shift to the Er^{3+} out-of-phase mode. Since it is always negative, this calculation cannot be used in the case of $-4z_{\text{Er}}J_{\text{Er}} < E_x + \mathfrak{g}_x^{\text{Er}}\mu_B B_x^{\text{DC}} < 4z_{\text{Er}}J_{\text{Er}}$. Such a situation corresponds to the Γ_{12} phase, and the present expression cannot be used.

In Figs. 6(a,c) and (b,d), we plot the spin resonance frequencies calculated by the mean-field approach, Eqs. (C1), and by Eqs. (C9) (solid lines) and (C10) (dashed lines), respectively. Due to the broken mirror symmetry of spins about the bc plane even in the absence of the DC field, the resonance frequencies depend on the sign of the DC field B_x^{DC} .

As shown by the dashed lines in Figs. 6(b,d), the Er^{3+} out-of-phase and Fe^{3+} qAFM modes show frequency anti-crossing around $B_x^{\text{DC}} = 13$ T and $B_x^{\text{DC}} = -14$ T obeying Eq. (C10). As shown by solid lines in Figs. 6(b,d), the anti-crossing between Er^{3+} in-phase and Fe^{3+} qFM modes clearly appears around $B_x^{\text{DC}} \sim -7$ T obeying Eq. (C9), while it is very small around $B_x^{\text{DC}} \sim 7$ T as shown in the insets. This is because the coupling strength $g_y + g'_z = 2\pi \times 7 \times 10^{-4}$ THz for the rotating terms ($\hat{a}_0^{\dagger}\hat{b}_{+} - \hat{b}_{+}^{\dagger}\hat{a}_0$) is small for $B_x^{\text{DC}} > 0$.

The frequency splitting between the in-phase and out-of-phase Er^{3+} resonances originates from the $\text{Er}^{3+}\text{-Er}^{3+}$ exchange interaction as explained above. At a fixed temperature $T = 20$ K, as we discussed also in our previous study [33], the effective density (ratio x) of Er^{3+} spins (involved with coherent dynamics such as spin precession) is decreased by decreasing the Er^{3+} excitation energy E_{Er} following Eq. (C3). Then, the splitting frequency $4z_{\text{Er}}J_{\text{Er}}$ is decreased by the decrease in $|B_x|$.

The two approaches (mean-field method and extended Dicke Hamiltonian) show almost the same resonance frequencies except the slight frequency blue-shift of the Fe^{3+} qFM mode at large $-B_x$. It is obtained by the mean-field approach but are not by the extended Dicke Hamiltonian. This shift of the Fe^{3+} magnon mode is due to the Zeeman effect (external DC field) in the Fe^{3+} subsystem and the influence from the macroscopic paramagnetic Er^{3+} spins. They are not considered in the present calculation with the extended Dicke Hamiltonian.

2. $B^{\text{DC}}//b$

When the external DC magnetic field along the b axis is large enough ($|\mathfrak{g}_y^{\text{Er}}\mu_B B_y^{\text{DC}}| \gg E_x$), the $E_x\hat{\Sigma}_x^+$ term in

Eq. (C2) can be neglected. In the same manner as the previous subsection, we transform the Er^{3+} spins as

$$\hat{\Sigma}_y^s \rightarrow \hat{b}_s^{\dagger}\hat{b}_s - \frac{N}{4}, \quad (\text{C11a})$$

$$\delta\hat{\Sigma}_y^s \rightarrow \hat{b}_s^{\dagger}\hat{b}_s, \quad (\text{C11b})$$

$$\hat{\Sigma}_z^s = \delta\hat{\Sigma}_z^s \rightarrow \sqrt{\frac{N}{2}}\frac{\hat{b}_s^{\dagger} + \hat{b}_s}{2}, \quad (\text{C11c})$$

$$\hat{\Sigma}_x^s = \delta\hat{\Sigma}_x^s \rightarrow \sqrt{\frac{N}{2}}\frac{\hat{b}_s^{\dagger} - \hat{b}_s}{i2}. \quad (\text{C11d})$$

Then, in the weak excitation limit, the total Hamiltonian in Eq. (C2) is transformed to

$$\begin{aligned} \hat{\mathcal{H}} &\approx \sum_{K=0,\pi} \hbar\omega_K \hat{a}_K^{\dagger}\hat{a}_K + |\mathfrak{g}_y^{\text{Er}}\mu_B B_y^{\text{DC}}|(\hat{b}_+^{\dagger}\hat{b}_+ + \hat{b}_-^{\dagger}\hat{b}_-) \\ &- 4z_{\text{Er}}J_{\text{Er}}\hat{b}_-^{\dagger}\hat{b}_- - i\hbar g_x(\hat{a}_{\pi}^{\dagger} + \hat{a}_{\pi})(\hat{b}_+^{\dagger} - \hat{b}_+) \\ &+ i\hbar g_z(\hat{a}_{\pi}^{\dagger} - \hat{a}_{\pi})(\hat{b}_-^{\dagger} + \hat{b}_-) + \hbar g'_z(\hat{a}_0^{\dagger} + \hat{a}_0)(\hat{b}_+^{\dagger} + \hat{b}_+) \\ &+ \text{const.} \quad (\text{C12}) \end{aligned}$$

This Hamiltonian can be used for $|\mathfrak{g}_y^{\text{Er}}\mu_B B_y^{\text{DC}}| > 4z_{\text{Er}}J_{\text{Er}}$ similarly as the previous subsection. In this configuration, the two Fe^{3+} magnon modes and two Er^{3+} modes are all coupled in general. However, when we focus around the Fe^{3+} qFM magnon frequency, the Hamiltonian can be simplified as

$$\begin{aligned} \hat{\mathcal{H}} &\approx \hbar\omega_0 \hat{a}_0^{\dagger}\hat{a}_0 + |\mathfrak{g}_y^{\text{Er}}\mu_B B_y^{\text{DC}}|\hat{b}_+^{\dagger}\hat{b}_+ \\ &+ \hbar g'_z(\hat{a}_0^{\dagger} + \hat{a}_0)(\hat{b}_+^{\dagger} + \hat{b}_+) + \text{const.} \quad (\text{C13a}) \end{aligned}$$

In this way, the Fe^{3+} qFM mode shows anti-crossing with the Er^{3+} in-phase mode. On the other hand, when we focus on the Fe^{3+} qAFM magnon mode, the Hamiltonian is simplified as

$$\begin{aligned} \hat{\mathcal{H}}_{\pi-} &\approx \hbar\omega_{\pi}\hat{a}_{\pi}^{\dagger}\hat{a}_{\pi} + (|\mathfrak{g}_y^{\text{Er}}\mu_B B_y^{\text{DC}}| - 4z_{\text{Er}}J_{\text{Er}})\hat{b}_-^{\dagger}\hat{b}_- \\ &+ |\mathfrak{g}_y^{\text{Er}}\mu_B B_y^{\text{DC}}|\hat{b}_+^{\dagger}\hat{b}_+ - i\hbar g_x(\hat{a}_{\pi}^{\dagger} + \hat{a}_{\pi})(\hat{b}_+^{\dagger} - \hat{b}_+) \\ &+ i\hbar g_z(\hat{a}_{\pi}^{\dagger} - \hat{a}_{\pi})(\hat{b}_-^{\dagger} + \hat{b}_-) + \text{const.} \quad (\text{C13b}) \end{aligned}$$

In this way, the Fe^{3+} qAFM mode shows anti-crossing with both Er^{3+} in-phase and out-of-phase modes.

In Figs. 7(a) and (b), we plot the spin resonance frequencies calculated by the mean-field approach, Eqs. (C1), and by Eq. (C12), respectively. The Er^{3+} in-phase and Fe^{3+} qFM modes show frequency anti-crossing around $B_y = 12$ T. The Fe^{3+} qAFM mode shows anti-crossing with the two Er^{3+} modes around $B_y = 20$ T. The two approaches show almost the same resonance frequencies in the present case.

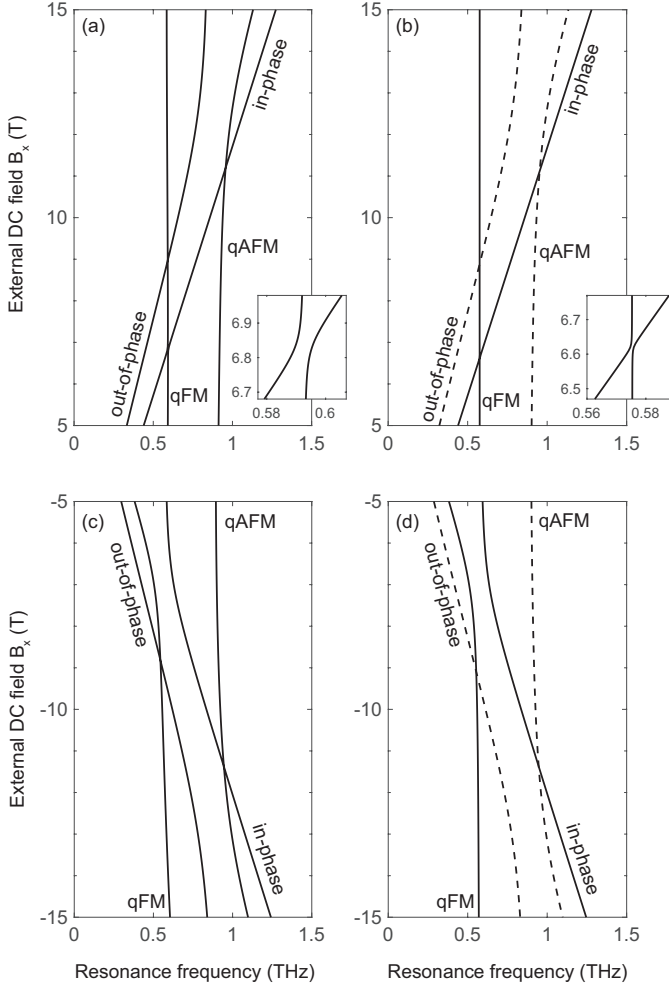


FIG. 6. Resonance frequencies of Er^{3+} and Fe^{3+} spins in ErFeO_3 at $T = 20$ K under an external DC magnetic field along the a axis for positive (a,b) and negative (c,d) directions. Figures 6(a,c) and (b,d) are calculated, respectively, by the mean-field approach, Eqs. (C1), and by the extended Dicke Hamiltonian, Eqs. (C9) (solid lines) and (C10) (dashed lines). The Er^{3+} out-of-phase and Fe^{3+} qAFM modes show frequency anti-crossing around $B_x = 13$ T and $B_x = -14$ T obeying Eq. (C10) (dashed lines in Figs. 6(b,d)). The anti-crossing between Er^{3+} in-phase and Fe^{3+} qFM modes is very small for positive B_x (solid lines in Fig. 6(b)) but is relatively large for negative B_x obeying Eq. (C9) (solid lines in Fig. 6(d)). The frequency splitting between the Er^{3+} in-phase and out-of-phase modes is narrowed at small $|B_x|$ due to the thermal excitation of Er^{3+} spins. The two approaches show almost the same resonance frequencies except the slight frequency blue-shift of the Fe^{3+} qFM mode at large $-B_x$. It is not obtained by the extended Dicke Hamiltonian due to the approximations used to derive it.

3. $B^{\text{DC}}//c$

Finally, when the external DC magnetic field along the c axis is large enough ($|\mathbf{g}_z^{\text{Er}} \mu_B B_z^{\text{DC}}| \gg E_x$), the $E_x \hat{\Sigma}_x^+$ term in Eq. (C2) can be neglected. In the same manner

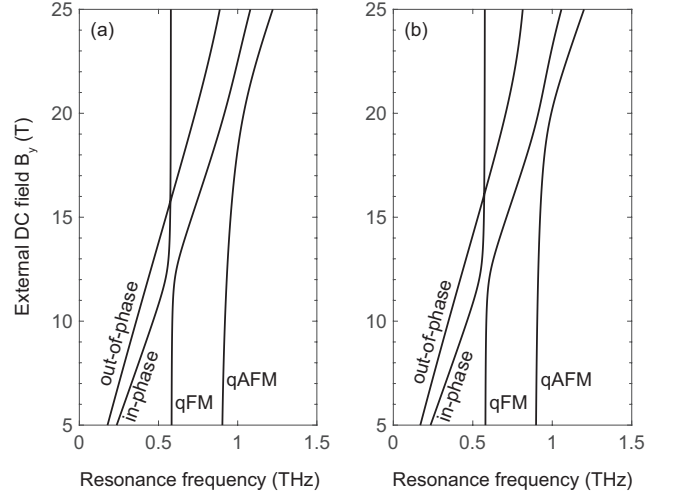


FIG. 7. Resonance frequencies of Er^{3+} and Fe^{3+} spins in ErFeO_3 at $T = 20$ K under an external DC magnetic field along the b axis. Figures 7(a) and (b) are calculated, respectively, by the mean-field approach, Eqs. (C1), and by the extended Dicke Hamiltonian, Eq. (C12). The Er^{3+} in-phase and Fe^{3+} qFM modes show frequency anti-crossing around $B_y = 12$ T and the Fe^{3+} qAFM mode shows anti-crossing with the two Er^{3+} modes around $B_y = 20$ T. The frequency splitting between the Er^{3+} in-phase and out-of-phase modes is narrowed at small $|B_y|$ due to the thermal excitation of Er^{3+} spins. The two approaches show almost the same resonance frequencies.

as the previous subsections, we transform the Er^{3+} spins as

$$\hat{\Sigma}_z^s = \hat{b}_s^\dagger \hat{b}_s - \frac{N}{4}, \quad (\text{C14a})$$

$$\delta \hat{\Sigma}_z^s = \hat{b}_s^\dagger \hat{b}_s, \quad (\text{C14b})$$

$$\hat{\Sigma}_x^s = \delta \hat{\Sigma}_x^s = \sqrt{\frac{N}{2}} \frac{\hat{b}_s^\dagger + \hat{b}_s}{2}, \quad (\text{C14c})$$

$$\hat{\Sigma}_y^s = \delta \hat{\Sigma}_y^s = \sqrt{\frac{N}{2}} \frac{\hat{b}_s^\dagger - \hat{b}_s}{i2}. \quad (\text{C14d})$$

In the weak excitation limit, the total Hamiltonian in Eq. (C2) is transformed to

$$\begin{aligned} \hat{\mathcal{H}} \approx & \sum_{K=0,\pi} \hbar \omega_K \hat{a}_K^\dagger \hat{a}_K + |\mathbf{g}_z^{\text{Er}} \mu_B B_z^{\text{DC}}| (\hat{b}_+^\dagger \hat{b}_+ + \hat{b}_-^\dagger \hat{b}_-) \\ & - 4z_{\text{Er}} J_{\text{Er}} \hat{b}_-^\dagger \hat{b}_- \\ & + \hbar g_x (\hat{a}_\pi^\dagger + \hat{a}_\pi) (\hat{b}_+^\dagger + \hat{b}_+) + \hbar g_y (\hat{a}_0^\dagger - \hat{a}_0) (\hat{b}_+^\dagger - \hat{b}_+) \\ & - i \hbar g'_y (\hat{a}_\pi^\dagger + \hat{a}_\pi) (\hat{b}_-^\dagger - \hat{b}_-) + \text{const.} \end{aligned} \quad (\text{C15})$$

This Hamiltonian can be used for $|\mathbf{g}_z^{\text{Er}} \mu_B B_z^{\text{DC}}| > 4z_{\text{Er}} J_{\text{Er}}$ similarly as the previous subsections. Also in this configuration, the two Fe^{3+} magnon modes and two Er^{3+} modes are all coupled. However, since $g'_y \ll g_x, g_y$, we can neglect the g'_y term. Then, the Hamiltonian is simplified as

$$\hat{\mathcal{H}} \approx \hat{\mathcal{H}}_{0\pi+} + \hat{\mathcal{H}}_- + \text{const.} \quad (\text{C16})$$

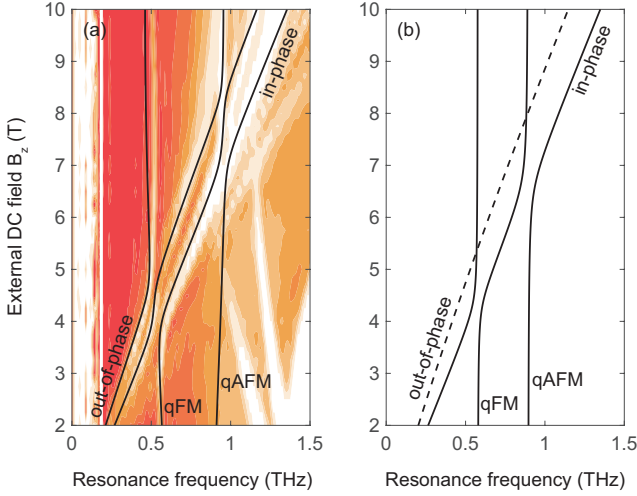


FIG. 8. Resonance frequencies of Er^{3+} and Fe^{3+} spins in ErFeO_3 at $T = 20$ K under an external DC magnetic field along the c axis. Figures 8(a) and (b) are calculated, respectively, by the mean-field approach, Eqs. (C1), and by the extended Dicke Hamiltonian, Eqs. (C17) (solid lines) and (C18) (dashed lines). The experimentally observed absorption spectrum [33] is plotted by red color in Fig. 8(a). The Er^{3+} in-phase mode shows frequency anti-crossing with Fe^{3+} qFM mode around $B_z = 4$ T and with qAFM mode around $B_z = 7$ T obeying Eq. (C17) (solid lines in Fig. 8(b)). The frequency splitting between the Er^{3+} in-phase and out-of-phase modes is narrowed at small $|B_y|$ due to the thermal excitation of Er^{3+} spins. In contrast to Figs. 6 ($\mathbf{B}^{\text{DC}}//a$) and 7 ($\mathbf{B}^{\text{DC}}//b$), the two results show an inconsistency concerning the anti-crossing between the Er^{3+} out-of-phase and the two Fe^{3+} magnon modes (around $B_z = 4.5$ T and 8.5 T). The reason is discussed at the end of Appendix C3. The frequency shifts of the Fe^{3+} qFM and qAFM modes at high external DC field are also not obtained by the extended Dicke Hamiltonian due to the approximations used to derive it.

The first term consists of the two Fe^{3+} magnon modes and the Er^{3+} in-phase mode as

$$\begin{aligned} \hat{\mathcal{H}}_{0\pi^+} \equiv & \sum_{K=0,\pi} \hbar\omega_K \hat{a}_0^\dagger \hat{a}_K + |\mathbf{g}_z^{\text{Er}} \mu_B B_z^{\text{DC}}| \hat{b}_+^\dagger \hat{b}_+ \\ & + \hbar g_y (\hat{a}_0^\dagger - \hat{a}_0) (\hat{b}_+^\dagger - \hat{b}_+) \\ & + \hbar g_x (\hat{a}_\pi^\dagger + \hat{a}_\pi) (\hat{b}_+^\dagger + \hat{b}_+). \end{aligned} \quad (\text{C17})$$

In this way, the Er^{3+} in-phase mode shows anti-crossing with both the two Fe^{3+} magnon modes. The second term in Eq. (C16) represents only the Er^{3+} out-of-phase mode as

$$\hat{\mathcal{H}}_- \equiv (|\mathbf{g}_z^{\text{Er}} \mu_B B_z^{\text{DC}}| - 4z_{\text{Er}} J_{\text{Er}}) \hat{b}_-^\dagger \hat{b}_-. \quad (\text{C18})$$

This mode is coupled only with the qAFM mode by the strength of $g'_y \ll g_x, g_y$ under the approximation used for deriving the extended Dicke Hamiltonian.

In Figs. 8(a) and (b), we plot the spin resonance frequencies calculated by the mean-field approach, Eqs. (C1), and by the extended Dicke Hamiltonian,

Eqs. (C17) (solid lines) and (C18) (dashed lines), respectively. As shown by solid lines in Fig. 8(b), obeying Eq. (C17), the Er^{3+} in-phase mode shows frequency anti-crossing with Fe^{3+} qFM mode around $B_z = 4$ T and with qAFM mode around $B_z = 7$ T. The frequency shifts of the Fe^{3+} magnon modes at large B_z are not reproduced in Fig. 8(b) due to the approximations explained at the end of Appendix C1.

As shown in Fig. 8(a), the Er^{3+} out-of-phase mode shows frequency anti-crossing with the Fe^{3+} qFM mode around $B_z = 4.5$ T and with the qAFM mode around $B_z = 8.5$ T. They are not obtained by the present calculation with the extended Dicke Hamiltonian as shown in Fig. 8(b). Such an inconsistency does not appear in the previous cases ($\mathbf{B}^{\text{DC}}//a, b$). We checked that the inconsistency cannot be resolved even by considering the equilibrium contribution $\bar{\Sigma}_{x,y,z}^\pm$ in the Er^{3+} -magnon couplings in Eq. (C2). The g'_y term also cannot resolve it, since it induces only the coupling between the Er^{3+} out-of-phase and Fe^{3+} qAFM modes.

This inconsistency originates from the fact that we did not properly consider the change of the equilibrium values of Er^{3+} and Fe^{3+} spins by the presence of the external DC field \mathbf{B}^{DC} in the derivation of the extended Dicke Hamiltonian. In fact, in the presence of $\mathbf{B}^{\text{DC}}//c$, we can find by the mean-field method that the Fe^{3+} spins become strongly asymmetric about the ab plane due to the large z component of the macroscopic Er^{3+} spins induced by $\mathbf{B}^{\text{DC}}//c$. Such an asymmetry causes the coupling between the Er^{3+} out-of-phase mode and the two Fe^{3+} magnon modes. Then, the anti-crossing appears in Fig. 8(a).

The reproduction of these anti-crossing by the extended Dicke Hamiltonian is beyond the scope of the present paper and it remains as a future task.

4. Comparison with experimental results

Since the maximum external DC magnetic flux density was limited by around 10 T in our previous study [33], the Er^{3+} -magnon anti-crossing was experimentally observed mainly for $\mathbf{B}^{\text{DC}}//c$. The anti-crossing around $B_z^{\text{DC}} = 4$ T (7 T) was clearly (slightly) observed. If we apply the external DC field in the anti-parallel direction to the magnetization along the a axis, we could observe anti-crossing around $B_x^{\text{DC}} = -7$ T as shown in Fig. 6. If we can apply a stronger DC magnetic field and the linewidth is narrow enough, we could observe the anti-crossing around $B_y^{\text{DC}} = 20$ T for $\mathbf{B}^{\text{DC}}//b$ as shown in Fig. 7. In our previous study [33], the anti-crossing was slightly observed around $B_y^{\text{DC}} = 7$ T. It corresponds to the one around $B_y^{\text{DC}} = 12$ T in Fig. 7. The difference between the theoretical and experimental external DC fields is due to the red-shift of Fe^{3+} qFM mode caused by the DC-field-induced structural change, which is not considered in the present calculation. For $\mathbf{B}^{\text{DC}}//a$, in order to observe the large anti-crossing around $B_x^{\text{DC}} = 13$ T and

–14 T in Fig. 6, the probe THz wave should be irradiated along the b or c axis, since the Fe^{3+} qAFM modes can be excited by the oscillating magnetic field only along the a axis.

As shown in Fig. 2, the phase diagrams around the LTPT of ErFeO_3 are well reproduced by the mean-field method with our spin model. Concerning other phase transitions at higher temperature and stronger DC field, the present spin model can reproduce the transition between the Γ_2 phase and the Γ_4 one, where the Fe^{3+} spins are ordered antiferromagnetically along the a axis with a slight canting to the c axis, in the case of $\mathbf{B}^{\text{DC}}//c$. It occurs around $B_z^{\text{DC}} \sim 20$ T [34]. However, the temperature-induced Γ_2 – Γ_4 spin-reorientation phase transition around $90 \text{ K} \lesssim T \lesssim 100 \text{ K}$ [34, 43, 44] cannot be reproduced in the present model. We need a more complicated spin model for the Fe^{3+} subsystem, [67–71] while it is beyond the scope of this paper. Further, the phase transitions around $B_x^{\text{DC}} = 15$ T for $\mathbf{B}^{\text{DC}}//a$ and $B_y^{\text{DC}} = 20$ T for $\mathbf{B}^{\text{DC}}//b$ reported by Zhang *et al.* [34] cannot also be reproduced in the present spin model. The reproduction of these phase transitions remains a future task. Existence of these transitions are the reason why we restrict $|B_x^{\text{DC}}| < 15$ T in Fig. 6 and $B_y^{\text{DC}} < 25$ T in Fig. 7, while we enlarged the latter range for clearly showing the anti-crossing around $B_y^{\text{DC}} = 20$ T.

Appendix D: Parameters

Following our previous study [33], we used the following values for the Fe^{3+} subsystem in our numerical calculations, except A_x , which was determined for fitting the spin resonance frequencies in Fig. 8 to the corresponding THz absorption spectrum in our experiments: [33]

$$J_{\text{Fe}} = 4.96 \text{ meV}, \quad (\text{D1a})$$

$$D_y^{\text{Fe}} = -0.107 \text{ meV}, \quad (\text{D1b})$$

$$A_x = 0.0073 \text{ meV}, \quad (\text{D1c})$$

$$A_z = 0.0150 \text{ meV}, \quad (\text{D1d})$$

$$A_{xz} = 0. \quad (\text{D1e})$$

The anisotropic g -factors for Er^{3+} spins were assumed to be

$$\mathbf{g}_x^{\text{Er}} = 6, \quad (\text{D2a})$$

$$\mathbf{g}_y^{\text{Er}} = 3.4, \quad (\text{D2b})$$

$$\mathbf{g}_z^{\text{Er}} = 9.6. \quad (\text{D2c})$$

They were determined for fitting the Er^{3+} spin resonance frequencies in Figs. 6, 7, and 8 to their absorption peak positions observed in our experiments [33]. They are basically multiplied by factor 2 from the values estimated in our previous study [33] due to the additional factor 1/2 in Eq. (13).

The anisotropic g -factors for Fe^{3+} spins were assumed to be

$$\mathbf{g}_x^{\text{Fe}} = 2, \quad (\text{D3a})$$

$$\mathbf{g}_y^{\text{Fe}} = 2, \quad (\text{D3b})$$

$$\mathbf{g}_z^{\text{Fe}} = 0.6. \quad (\text{D3c})$$

Here, \mathbf{g}_z^{Fe} was determined for reproducing the critical magnetic flux density $B_z^{\text{DC}} \sim 20$ T [34] of the transition between the Γ_2 phase and the Γ_4 one, where the Fe^{3+} spins are ordered antiferromagnetically along the a axis with a slight canting to the c axis, in the case of $\mathbf{B}^{\text{DC}}//c$. On the other hand, \mathbf{g}_x^{Fe} and \mathbf{g}_y^{Fe} were simply set to be that of the free electron spin, since the results in the present paper is very insensitive to these values.

Concerning the Er^{3+} – Er^{3+} and Er^{3+} – Fe^{3+} exchange interactions, we used the following values:

$$J_{\text{Er}} = 0.037 \text{ meV} \quad (\text{D4a})$$

$$J = 0.60 \text{ meV} \quad (\text{D4b})$$

$$D_x = 0.034 \text{ meV} \quad (\text{D4c})$$

$$D_y = 0.003 \text{ meV} \quad (\text{D4d})$$

They were roughly determined for fitting Figs. 2 to the phase diagrams reported by Zhang *et al.* [34]. The precise values of J_{Er} , J , and D_y were mainly determined for fitting our calculated spin resonance frequencies for $\mathbf{B}^{\text{DC}}//c$ to the corresponding THz absorption spectrum in our experiments [33], which are both shown in Fig. 8(a). On the other hand, D_x was determined for reproducing the critical temperature $T_c = 4.0$ K.

Although the ratio between the Er^{3+} – Er^{3+} and Er^{3+} – Fe^{3+} interaction strengths was theoretically investigated by the phase boundary for $\mathbf{B}^{\text{DC}}//a$ [46], the phase diagrams (critical temperature and DC fields) themselves were not enough at least for determining all our parameters, while we do not intend to scientifically claim its impossibility in this paper. As far as we tried, the phase diagrams give only some ranges of the parameters. Since the LTPT is caused not only by the Er^{3+} – Er^{3+} exchange interaction but also by the Er^{3+} – Fe^{3+} ones, there are at least four parameters J_{Er} , J , D_x , and D_y even if we reduce the number of parameters by the analysis in Appendix B. Further, the anisotropic g -factors \mathbf{g}_x^{Er} , \mathbf{g}_y^{Er} , and \mathbf{g}_z^{Er} of Er^{3+} spins were also free parameters, and they can easily change the critical DC fields. The critical temperature and the three critical DC fields obtained by the magnetization measurements were not enough for determining the above parameters.

In order to determine all of them, the spin resonance frequencies are informative. Especially, as we discussed in Appendix C by the extended Dicke Hamiltonian, the Er^{3+} – Er^{3+} exchange interaction strength J_{Er} clearly appears as the frequency splitting between the Er^{3+} in-phase and out-of-phase resonances. The out-of-phase mode cannot be excited by the THz wave unless it couples with the Fe^{3+} magnon modes. In that sense, the

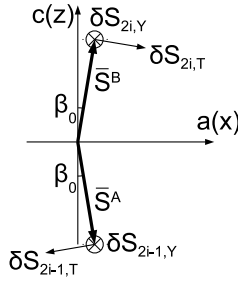


FIG. 9. Definitions of spin fluctuations $\delta\hat{S}_{\ell,T/Y}$. The index $\ell = 2i - 1$ and $2i$ correspond to the spins at the i -th site in the A and B sublattices, respectively.

anti-crossing between the Er^{3+} in-phase, out-of-phase resonances, and the Fe^{3+} qFM magnon mode around $B_z^{\text{DC}} \sim 4$ T in Fig. 8 gave the most fruitful information for determining J_{Er} and other parameters.

Appendix E: Magnon quantization

Here, we rewrite the Hamiltonian of Fe^{3+} spins described by $\hat{\mathcal{H}}_{\text{Fe}}$ in Eq. (8) in terms of the annihilation and creation operators of a magnon. As shown in Fig. 9, we define the modulations $\{\delta\hat{S}_{\ell,T}, \delta\hat{S}_{\ell,Y}\}$ of Fe^{3+} spins from their most stable values $\bar{\mathbf{S}}^{A/B}$ in its subsystem. The index $\ell = 2i - 1$ and $2i$ correspond to the spins at the i -th site in the A and B sublattices, respectively. The spin modulations are expressed in the original axes as

$$\delta\hat{\mathbf{S}}_i^A = \hat{\mathbf{S}}_i^A - \bar{\mathbf{S}}_i^A = \sqrt{S} \begin{pmatrix} -\delta\hat{S}_{2i-1,T} \cos \beta_0 \\ \delta\hat{S}_{2i-1,Y} \\ -\delta\hat{S}_{2i-1,T} \sin \beta_0 \end{pmatrix}, \quad (\text{E1a})$$

$$\delta\hat{\mathbf{S}}_i^B = \hat{\mathbf{S}}_i^B - \bar{\mathbf{S}}_i^B = \sqrt{S} \begin{pmatrix} \delta\hat{S}_{2i,T} \cos \beta_0 \\ \delta\hat{S}_{2i,Y} \\ -\delta\hat{S}_{2i,T} \sin \beta_0 \end{pmatrix}. \quad (\text{E1b})$$

The factor \sqrt{S} appears by considering the consistency with the Holstein–Primakoff transformation, while this factor did not appear in our previous studies, [33, 54] since the Fe^{3+} spins are normalized based on Herrmann’s calculation [53].

In the weak excitation limit, the spin fluctuations can be approximated as bosons (magnons), and we define a bosonic commutation relations for these modulations as

$$[\delta\hat{S}_{\ell,T}, \delta\hat{S}_{\ell',Y}] = i\delta_{\ell,\ell'}, \quad (\text{E2a})$$

$$[\delta\hat{S}_{\ell,T}, \delta\hat{S}_{\ell',T}] = [\delta\hat{S}_{\ell,Y}, \delta\hat{S}_{\ell',Y}] = 0. \quad (\text{E2b})$$

Extending Herrmann’s calculation into a magnon model propagating in the z direction (under averaging in the x - y plane) [72], we can derive the equations of motion

for these modulations as

$$\frac{1}{\gamma} \frac{\partial}{\partial t} \delta\hat{S}_{\ell,T} = -a\delta\hat{S}_{\ell,Y} + \frac{b}{2} (\delta\hat{S}_{\ell-1,Y} + \delta\hat{S}_{\ell+1,Y}), \quad (\text{E3a})$$

$$\frac{1}{\gamma} \frac{\partial}{\partial t} \delta\hat{S}_{\ell,Y} = -c\delta\hat{S}_{\ell,T} - \frac{d}{2} (\delta\hat{S}_{\ell-1,T} + \delta\hat{S}_{\ell+1,T}). \quad (\text{E3b})$$

Here, $\gamma = \mathbf{g}\mu_B/\hbar$ is the gyromagnetic ratio for the free electron g -factor \mathbf{g} and the Bohr magneton μ_B . The coefficients a , b , c , and d are defined in Eqs. (22) [53]. Then, the Hamiltonian of the Fe^{3+} spins is approximated (bosonized) as

$$\hat{\mathcal{H}}_{\text{Fe}} \approx \hbar\gamma \sum_{\ell=1}^{2N_z} \left(-\frac{a}{2} \delta\hat{S}_{\ell,Y}^2 + \frac{c}{2} \delta\hat{S}_{\ell,T}^2 + \frac{b}{2} \delta\hat{S}_{\ell,Y} \delta\hat{S}_{\ell+1,Y} + \frac{d}{2} \delta\hat{S}_{\ell,T} \delta\hat{S}_{\ell+1,T} \right) + \text{const.} \quad (\text{E4})$$

Here, N_z and $2N_z$ are the number of unit cells and of Fe^{3+} spins, respectively, in the z direction. In terms of the annihilation operator \hat{a}_K of a magnon with a dimensionless wavenumber K , satisfying $[\hat{a}_K, \hat{a}_{K'}^\dagger] = \delta_{K,K'}$, the modulation operators are expressed as

$$\delta\hat{S}_{\ell,T} = \frac{1}{\sqrt{2N_z}} \sum_{K=-\pi}^{\pi} e^{iK\ell} \hat{T}_K, \quad (\text{E5a})$$

$$\delta\hat{S}_{\ell,Y} = \frac{1}{\sqrt{2N_z}} \sum_{K=-\pi}^{\pi} e^{iK\ell} \hat{Y}_K, \quad (\text{E5b})$$

$$\hat{T}_K = \left(\frac{b \cos K - a}{d \cos K + c} \right)^{1/4} \frac{(\hat{a}_{-K}^\dagger + \hat{a}_K)}{\sqrt{2}}, \quad (\text{E6a})$$

$$\hat{Y}_K = \left(\frac{d \cos K + c}{b \cos K - a} \right)^{1/4} \frac{i(\hat{a}_{-K}^\dagger - \hat{a}_K)}{\sqrt{2}}. \quad (\text{E6b})$$

The Hamiltonian in Eq. (E4) is rewritten as

$$\hat{\mathcal{H}}_{\text{Fe}} \approx \sum_K \hbar\omega_K \left(\hat{a}_K^\dagger \hat{a}_K + \frac{1}{2} \right) + \text{const.} \quad (\text{E7})$$

Since we want to discuss a phase transition where spin configurations are changed homogeneously in space (we set the same assumption in the mean-field calculation), we focus on only the two modes with $K = 0$ and π . Then, the above Hamiltonian is approximated to Eq. (20). The fluctuations are approximated as

$$\delta\hat{S}_{2\ell-1,T} \approx \frac{1}{\sqrt{2N_z}} (\hat{T}_0 - \hat{T}_\pi), \quad (\text{E8a})$$

$$\delta\hat{S}_{2\ell-1,Y} \approx \frac{1}{\sqrt{2N_z}} (\hat{Y}_0 - \hat{Y}_\pi), \quad (\text{E8b})$$

$$\delta\hat{S}_{2\ell,T} \approx \frac{1}{\sqrt{2N_z}} (\hat{T}_0 + \hat{T}_\pi), \quad (\text{E8c})$$

$$\delta\hat{S}_{2\ell,Y} \approx \frac{1}{\sqrt{2N_z}} (\hat{Y}_0 + \hat{Y}_\pi). \quad (\text{E8d})$$

Under this approximation, the fluctuations do not depend on the index ℓ of unit cell. In the original xyz -axes shown in Fig. 9, the fluctuation vectors are expressed in Eqs. (23).

Appendix F: Aspects of phase boundaries

In Fig. 5, the phase boundaries obtained by the two approaches show small differences. The dash-dotted curves (phase transition only by the Er^{3+} - Er^{3+} exchange interaction) are almost the same. However, the solid and dashed curves by the extended Dicke Hamiltonian are shifted to the positive side from those obtained by the mean-field approach. These shifts of the critical magnetic fields are mainly due to the neglect of \mathbf{B}^{DC} -dependence of Fe^{3+} spins in the derivation of the extended Dicke Hamiltonian. Then, a more sophisticated derivation of

the extended Dicke Hamiltonian will resolve these differences, while it is beyond the scope of the present paper.

Note also that, in both approaches, the absolute values of the negative critical fields are larger than the positive ones for the solid and dash-dotted curves, while they are almost the same (symmetric about the origin) for the dashed curves. The symmetric phase boundary is obtained because the Er^{3+} spins are not influenced by the weak magnetization of Fe^{3+} spins in the absence of the Er^{3+} - Fe^{3+} exchange interactions (Er^{3+} -magnon couplings). In contrast, the phase boundaries become asymmetric about the origin in the presence of the Er^{3+} - Fe^{3+} exchange interactions (Er^{3+} -magnon couplings). It is for compensating the magnetization along the a axis.

-
- [1] K. Hepp and E. H. Lieb, On the superradiant phase transition for molecules in a quantized radiation field: the dicke maser model, *Ann. Phys. (N. Y.)* **76**, 360 (1973).
- [2] Y. K. Wang and F. T. Hioe, Phase transition in the dicke model of superradiance, *Phys. Rev. A* **7**, 831 (1973).
- [3] C. Ciuti, G. Bastard, and I. Carusotto, Quantum vacuum properties of the intersubband cavity polariton field, *Phys. Rev. B* **72**, 115303 (2005).
- [4] P. Forn-Díaz, L. Lamata, E. Rico, J. Kono, and E. Solano, Ultrastrong coupling regimes of light-matter interaction, *Rev. Mod. Phys.* **91**, 025005 (2019).
- [5] A. Frisk Kockum, A. Miranowicz, S. De Liberato, S. Savasta, and F. Nori, Ultrastrong coupling between light and matter, *Nat. Rev. Phys.* **1**, 19 (2019).
- [6] R. H. Dicke, Coherence in spontaneous radiation processes, *Phys. Rev.* **93**, 99 (1954).
- [7] K. Baumann, C. Guerlin, F. Brennecke, and T. Esslinger, Dicke quantum phase transition with a superfluid gas in an optical cavity, *Nature* **464**, 1301 (2010).
- [8] P. Kirton, M. M. Roses, J. Keeling, and E. G. Dalla Torre, Introduction to the Dicke Model: From Equilibrium to Nonequilibrium, and Vice Versa, *Adv. Quantum Technol.* **2**, 1800043 (2019).
- [9] M. Bamba, K. Inomata, and Y. Nakamura, Superradiant Phase Transition in a Superconducting Circuit in Thermal Equilibrium, *Phys. Rev. Lett.* **117**, 173601 (2016).
- [10] K. Rzążewski, K. Wódkiewicz, and W. Żakowicz, Phase Transitions, Two-Level Atoms, and the $\$A^2\$$ Term, *Phys. Rev. Lett.* **35**, 432 (1975).
- [11] J. M. Knight, Y. Aharonov, and G. T. C. Hsieh, Are super-radiant phase transitions possible?, *Phys. Rev. A* **17**, 1454 (1978).
- [12] I. Bialynicki-Birula and K. Rzążewski, No-go theorem concerning the superradiant phase transition in atomic systems, *Phys. Rev. A* **19**, 301 (1979).
- [13] K. Gawędzki and K. Rzążewski, No-go theorem for the superradiant phase transition without dipole approximation, *Phys. Rev. A* **23**, 2134 (1981).
- [14] K. Hepp, E. H. Lieb, R. Field, and K. Etudes, Equilibrium Statistical Mechanics of Matter Interacting with the Quantized Radiation Field, *Phys. Rev. A* **8**, 2517 (1973).
- [15] J. L. van Hemmen and K. Rzążewski, On the thermodynamic equivalence of the Dicke maser model and a certain spin system, *Phys. Lett. A* **77**, 211 (1980).
- [16] M. Bamba and N. Imoto, Circuit configurations which may or may not show superradiant phase transitions, *Phys. Rev. A* **96**, 053857 (2017).
- [17] J. Keeling, Coulomb interactions, gauge invariance, and phase transitions of the Dicke model, *J. Phys. Condens. Matter* **19**, 295213 (2007).
- [18] A. Vukics and P. Domokos, Adequacy of the Dicke model in cavity QED: A counter-no-go statement, *Phys. Rev. A* **86**, 53807 (2012).
- [19] A. Vukics, T. Grieser, and P. Domokos, Elimination of the A-square problem from cavity QED, *Phys. Rev. Lett.* **112**, 73601 (2014).
- [20] M. Bamba and T. Ogawa, Stability of polarizable materials against superradiant phase transition, *Phys. Rev. A* **90**, 063825 (2014).
- [21] A. Vukics, T. Grieser, and P. Domokos, Fundamental limitation of ultrastrong coupling between light and atoms, *Phys. Rev. A* **92**, 43835 (2015).
- [22] T. Grieser, A. Vukics, and P. Domokos, Depolarization shift of the superradiant phase transition, *Phys. Rev. A* **94**, 033815 (2016).
- [23] D. Hagenmüller and C. Ciuti, Cavity QED of the graphene cyclotron transition, *Phys. Rev. Lett.* **109**, 267403 (2012).
- [24] L. Chirolli, M. Polini, V. Giovannetti, and A. H. MacDonald, Drude weight, cyclotron resonance, and the dicke model of graphene cavity QED, *Phys. Rev. Lett.* **109**, 267404 (2012).
- [25] G. Mazza and A. Georges, Superradiant Quantum Materials, *Phys. Rev. Lett.* **122**, 017401 (2019).
- [26] G. M. Andolina, F. M. D. Pellegrino, V. Giovannetti, A. H. MacDonald, and M. Polini, Cavity quantum electrodynamics of strongly correlated electron systems: A no-go theorem for photon condensation, *Phys. Rev. B* **100**, 121109 (2019).
- [27] P. Nataf, T. Champel, G. Blatter, and D. M. Basko, Rashba Cavity QED: A Route Towards the Superradiant Quantum Phase Transition, *Phys. Rev. Lett.* **123**, 207402 (2019).
- [28] X. Zhang, C. L. Zou, L. Jiang, and H. X. Tang, Strongly coupled magnons and cavity microwave photons, *Phys. Rev. Lett.* **113**, 156401 (2014).
- [29] M. Goryachev, W. G. Farr, D. L. Creedon, Y. Fan,

- M. Kostylev, and M. E. Tobar, High-cooperativity cavity QED with magnons at microwave frequencies, *Phys. Rev. Appl.* **2**, 54002 (2014).
- [30] J. Bourhill, N. Kostylev, M. Goryachev, D. L. Creedon, and M. E. Tobar, Ultrahigh cooperativity interactions between magnons and resonant photons in a YIG sphere, *Phys. Rev. B* **93**, 1 (2016).
- [31] N. Kostylev, M. Goryachev, and M. E. Tobar, Superstrong coupling of a microwave cavity to yttrium iron garnet magnons, *Appl. Phys. Lett.* **108** (2016).
- [32] G. Flower, M. Goryachev, J. Bourhill, and M. E. Tobar, Experimental implementations of cavity-magnon systems: From ultra strong coupling to applications in precision measurement, *New J. Phys.* **21**, 095004 (2019).
- [33] X. Li, M. Bamba, N. Yuan, Q. Zhang, Y. Zhao, M. Xiang, K. Xu, Z. Jin, W. Ren, G. Ma, S. Cao, D. Turchinovich, and J. Kono, Observation of Dicke cooperativity in magnetic interactions, *Science* (80-.). **361**, 794 (2018).
- [34] X. X. Zhang, Z. C. Xia, Y. J. Ke, X. Q. Zhang, Z. H. Cheng, Z. W. Ouyang, J. F. Wang, S. Huang, F. Yang, Y. J. Song, G. L. Xiao, H. Deng, and D. Q. Jiang, Magnetic behavior and complete high-field magnetic phase diagram of the orthoferrite ErFeO₃, *Phys. Rev. B* **100**, 054418 (2019).
- [35] Y. Tabuchi, S. Ishino, T. Ishikawa, R. Yamazaki, K. Usami, and Y. Nakamura, Hybridizing ferromagnetic magnons and microwave photons in the quantum limit, *Phys. Rev. Lett.* **113**, 83603 (2014).
- [36] Y. Tabuchi, S. Ishino, A. Noguchi, T. Ishikawa, R. Yamazaki, K. Usami, and Y. Nakamura, Coherent coupling between a ferromagnetic magnon and a superconducting qubit, *Science* (80-.). **349**, 405 (2015).
- [37] Y. Tabuchi, S. Ishino, A. Noguchi, T. Ishikawa, R. Yamazaki, K. Usami, and Y. Nakamura, La magnonique des quanta: Le magnon rencontre le qubit supraconducteur, *Comptes Rendus Phys.* **17**, 729 (2016).
- [38] R. G. Morris, A. F. Van Loo, S. Kosen, and A. D. Karenowska, Strong coupling of magnons in a YIG sphere to photons in a planar superconducting resonator in the quantum limit, *Sci. Rep.* **7**, 1 (2017).
- [39] G. Flower, J. Bourhill, M. Goryachev, and M. E. Tobar, Broadening frequency range of a ferromagnetic axion haloscope with strongly coupled cavity-magnon polaritons, *Phys. Dark Universe* **25**, 100306 (2019).
- [40] D. Macneill, J. T. Hou, D. R. Klein, P. Zhang, P. Jarillo-Herrero, and L. Liu, Gigahertz Frequency Antiferromagnetic Resonance and Strong Magnon-Magnon Coupling in the Layered Crystal CrCl₃, *Phys. Rev. Lett.* **123**, 47204 (2019).
- [41] L. Liensberger, A. Kamra, H. Maier-Flaig, S. Geprägs, A. Erb, S. T. B. Goennenwein, R. Gross, W. Belzig, H. Huebl, and M. Weiler, Exchange-enhanced Ultrastrong Magnon-Magnon Coupling in a Compensated Ferromagnet, *Phys. Rev. Lett.* **123**, 117204 (2019).
- [42] D. Lachance-Quirion, S. P. Wolski, Y. Tabuchi, S. Kono, K. Usami, and Y. Nakamura, Entanglement-based single-shot detection of a single magnon with a superconducting qubit, *Science* (80-.). **367**, 425 (2020).
- [43] G. Gorodetsky, R. M. Hornreich, I. Yaeger, H. Pinto, G. Shachar, and H. Shaked, Magnetic Structure of ErFeO₃ below 4.5 K, *Phys. Rev. B* **8**, 3398 (1973).
- [44] V. A. Klochov, N. M. Kovtun, and V. M. Khmara, Low-temperature spin configuration of iron ions in erbium orthoferrite, *Zh. Eksp. Teor. Fiz.* **68**, 721 (1975).
- [45] I. M. Vitebskii and D. A. Yablonskii, Theory of Low-Temperature Spin Reorientation in ErFeO₃, *Sov. Phys. Solid State* **20**, 1327 (1978).
- [46] A. M. Kadomtseva, I. B. Krynetskii, and V. M. Matveev, Nature of the spontaneous and field-induced low-temperature orientational transitions in erbium orthoferrite, *Sov. Phys. JETP* **52**, 732 (1980).
- [47] G. A. Gehring and K. A. Gehring, Co-operative Jahn-Teller effects, *Reports Prog. Phys.* **38**, 1 (1975).
- [48] K. I. Kugel' and D. I. Khomski, The Jahn-Teller effect and magnetism: transition metal compounds, *Sov. Phys. Uspekhi* **25**, 231 (1982).
- [49] J. Loos, On the Fluctuations and Phase Transitions in Dicke-Like Models, *Phys. status solidi* **123**, 595 (1984).
- [50] J. Larson, Jahn-Teller systems from a cavity QED perspective, *Phys. Rev. A* **78**, 33833 (2008).
- [51] G. F. Herrmann, Magnetic Resonances and Susceptibility in Orthoferrites, *Phys. Rev.* **133**, A1334 (1964).
- [52] D. L. Wood, J. P. Remeika, L. M. Holmes, and E. M. Gyorgy, Effect of Y and Bi Substitution on Spin Reorientation and Optical Absorption in ErFeO₃, *J. Appl. Phys.* **40**, 1245 (1969).
- [53] G. Herrmann, Resonance and high frequency susceptibility in canted antiferromagnetic substances, *J. Phys. Chem. Solids* **24**, 597 (1963).
- [54] M. Bamba, X. Li, and J. Kono, Terahertz strong-field physics without a strong external terahertz field, in *Ultrafast Phenom. Nanophotonics XXIII*, edited by M. Betz and A. Y. Elezzabi, SPIE, 2019, p. 5.
- [55] T. Holstein and H. Primakoff, Field Dependence of the Intrinsic Domain Magnetization of a Ferromagnet, *Phys. Rev.* **58**, 1098 (1940).
- [56] C. Emary and T. Brandes, Quantum Chaos Triggered by Precursors of a Quantum Phase Transition: The Dicke Model, *Phys. Rev. Lett.* **90**, 044101 (2003).
- [57] C. Emary and T. Brandes, Chaos and the quantum phase transition in the Dicke model, *Phys. Rev. E* **67**, 066203 (2003).
- [58] J. Larson and E. K. Irish, Some remarks on 'superradiant' phase transitions in light-matter systems, *J. Phys. A Math. Theor.* **50**, 174002 (2017).
- [59] D. S. Shapiro, W. V. Pogosov, and Y. E. Lozovik, Hierarchy of universal behaviors in generalized Dicke model near the superradiant phase transition , 1 (2019).
- [60] M. Artoni and J. L. Birman, Quantum-optical properties of polariton waves, *Phys. Rev. B* **44**, 3736 (1991).
- [61] M. Artoni and J. L. Birman, Polariton squeezing: theory and proposed experiment, *Quantum Opt. J. Eur. Opt. Soc. Part B* **1**, 91 (1989).
- [62] P. Schwendimann and A. Quattropani, Non-classical Properties of Polariton States, *Europhys. Lett.* **17**, 355 (1992).
- [63] P. Schwendimann and A. Quattropani, Non-classical Properties of Polariton States, *Europhys. Lett.* **18**, 281 (1992).
- [64] A. Quattropani and P. Schwendimann, Polariton squeezing in microcavities, *Phys. status solidi* **242**, 2302 (2005).
- [65] T. Makihara, K. Hayashida, G. T. Noe II, X. Li, N. M. Peraca, X. Ma, Z. Jin, W. Ren, G. Ma, I. Katayama, J. Takeda, H. Nojiri, D. Turchinovich, S. Cao, M. Bamba, and J. Kono, under reviewing (2020).
- [66] N. Marquez Peraca, X. Li, M. Bamba, C.-L. Huang, N. Yuan, X. Ma, G. T. Noe II, E. Morosan, S. Cao,

- and J. Kono, Terahertz Magnon Spectroscopy Mapping of the Low-Temperature Phases of $\text{Er}_x\text{Y}_{1-x}\text{FeO}_3$, Proceedings of 2020 Conference on Lasers and Electro-Optics (CLEO), FM4D.5.
- [67] J. R. Shane, Resonance frequencies of the orthoferrites in the spin reorientation region, *Phys. Rev. Lett.* **20**, 728 (1968).
- [68] L. M. Levinson, M. Luban, and S. Shtrikman, Microscopic model for reorientation of the easy axis of magnetization, *Phys. Rev.* **187**, 715 (1969).
- [69] T. Yamaguchi, Theory of spin reorientation in rare-earth orthochromites and orthoferrites, *J. Phys. Chem. Solids* **35**, 479 (1974).
- [70] A. M. Balbashov, G. V. Kozlov, A. A. Mukhin, and A. S. Prokhorov, Submillimeter Spectroscopy of Antiferromagnetic Dielectrics: Rare-Earth Orthoferrites, in *High Freq. Process. Magn. Mater.* (World Scientific, 1995), pp. 56–98.
- [71] E. E. Zubov, V. Markovich, I. Fita, A. Wisniewski, and R. Puzniak, Magnetic order in ErFeO_3 single crystals studied by mean-field theory, *Phys. Rev. B* **99**, 1 (2019).
- [72] C. H. Tsang, R. L. White, and R. M. White, Spin-wave damping of domain walls in YFeO_3 , *J. Appl. Phys.* **49**, 6063 (1978).